

## REVIEW

## Unconventional aspects of electronic transport in delafossite oxides

Ramzy Daou<sup>a</sup>, Raymond Frésard<sup>a</sup>, Volker Eyert<sup>a,b</sup>, Sylvie Hébert<sup>a</sup>, and Antoine Maignan<sup>a</sup>

Normandie Univ, ENSICAEN, UNICAEN, CNRS, CRISMAT, 14050 Caen, France; <sup>b</sup>Present address: Materials Design SARL, 42, Avenue Verdier, 92120 Montrouge, France

## ARTICLE HISTORY

Compiled March 8, 2024

## ABSTRACT

The electronic transport properties of the delafossite oxides  $ABO_2$  are usually understood in terms of two well separated entities, namely, the triangular  $A^+$  and  $(BO_2)^-$  layers. Here we review several cases among this extensive family of materials where the transport depends on the interlayer coupling and displays unconventional properties. We review the doped thermoelectrics based on  $CuRhO_2$  and  $CuCrO_2$ , which show a high-temperature recovery of Fermi-liquid transport exponents, as well as the highly anisotropic metals  $PdCoO_2$ ,  $PtCoO_2$  and  $PdCrO_2$  where the sheer simplicity of the Fermi surface leads to unconventional transport. We present some of the theoretical tools that have been used to investigate these transport properties and review what can and cannot be learned from the extensive set of electronic structure calculations that have been performed.

## KEYWORDS

Delafossites, resistivity, thermopower, Nernst effect, electronic structure, anisotropic materials, magnetism

## 1. Introduction

Transition metal oxides attract a lot of attention due to a great variety of physical phenomena, most of which go along with the ordering of some microscopic degrees of freedom as a function of, *e.g.*, temperature, pressure, or doping [1]. Prominent examples are the striking metal-insulator transitions in vanadium sesquioxide [2–5], high- $T_c$  superconductivity in the cuprates, or the colossal magnetoresistance observed in the manganates [6–9]. Cobaltates have aroused much interest due to the occurrence of different spin states [10–12]. In addition, they are promising materials for thermoelectric applications [13,14].

Known since 1873, when Friedel discovered the mineral  $CuFeO_2$  [15], the delafossites  $ABO_2$  continue to generate strong and ever increasing interest [16–18], especially after Kawazoe *et al.* showed simultaneous transparency and p-type conductivity [19] in  $CuAlO_2$ . This discovery laid the groundwork for the development of transparent optoelectronic devices. Furthermore, the quasi two-dimensionality of the lattice and the triangular coordination of atoms give rise to exciting physical properties such as strong anisotropy of the electrical conductivity and magnetic frustration effects.

---

Email: Raymond.Fresard@ensicaen.fr

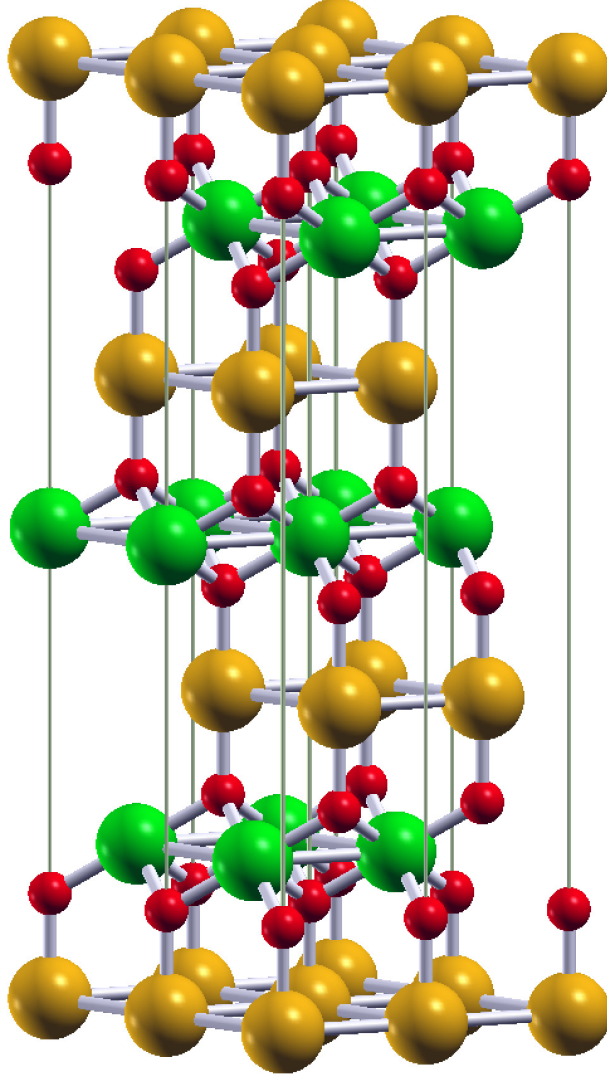


**Figure 1.** Crystal structure of delafossite  $ABO_2$ . A, B, and oxygen atoms are shown as orange, green, and red (light, big dark, and small dark in grayscale) spheres, respectively.

The delafossite structure has the space group  $R\bar{3}m$  and results from a stacking of monoatomic triangular layers, see Fig. 1 [16,18]. In particular, the B-atoms are at the centers of edge-sharing distorted oxygen octahedra, which form the characteristic  $BO_2$  sandwich layers. These trilayers are interlinked by linear O–A–O bonds, resulting in a twofold coordination of the A-atoms. However, the latter have, in addition, six in-plane nearest neighbor A-atoms. For this reason, the structure may be likewise regarded as formed from single A-atom layers, which are intertwined by the octahedral sandwiches. We find this point of view particularly useful when investigating the metallic delafossites. Finally, the oxygen atoms are tetrahedrally coordinated by one A-atom and three B-atoms. Pressure studies on  $PdCoO_2$  and  $PtCoO_2$  reveal an increase of the structural anisotropy on compression indicating the high mechanical stability of both the octahedral sandwich layers and the O–Pd–O (O–Pt–O) dumbbells [20].

Generically, the A and B atoms are mono- and trivalent, respectively. Depending

on the chemical composition, a wide variety of behaviors is therefore possible. For instance, if the  $A^+$  ion is in a  $d^9$  configuration, metallic conductivity is observed as in the case of  $\text{PdCoO}_2$ . If it is in a  $d^{10}$  configuration, the degrees of freedom dominating the low-energy physics can be traced back to the B atoms as, *e.g.*, in  $\text{CuCrO}_2$ ,  $\text{AgNiO}_2$  [21,22] and  $\text{AgCrO}_2$  [23,24].

In general, interest in the delafossite-type compounds has focused on the triangular arrangement of the transition-metal atoms and the resulting possible frustration effects, which arise once localized magnetic moments are established. While most of these oxides have been found to be antiferromagnetic semiconductors, other class members like  $\text{PdCrO}_2$ ,  $\text{PdCoO}_2$ ,  $\text{PdRhO}_2$ , and  $\text{PtCoO}_2$  attracted interest due to their rather high metallic conductivity. In particular,  $\text{PdCoO}_2$  has been shown to possess one of the lowest electric resistivities of normal-state oxides, even lower than that of Pd metal at room temperature [16,17,25]. In fact, with  $\rho(300\text{ K}) \simeq 2.6\ \mu\Omega\text{ cm}$  it is even comparable to pure Au. Yet, the conductivity is strongly anisotropic [16,25]. In particular, the ratio of the resistivities parallel and perpendicular to the  $c$  axis can be 400 or more in  $\text{PdCoO}_2$  [25,26].

Despite their simple chemical formulae the delafossites may be regarded as prototypical superlattices where the composition of both the A and B layers can be used to strongly influence the behavior of the whole system. For instance, in  $\text{CuCrO}_2$ , the Fermi energy falls into the Cr 3d band, but since the Cr layers order magnetically this compound is a magnetic semiconductor. In contrast, as will be shown below, in  $\text{PdCoO}_2$ , the Co layers only act as charge reservoirs, and conduction takes place almost exclusively in the Pd layers.

The paper is organized as follows: The experimental results on thermoelectric delafossites  $\text{CuCr}_{1-x}\text{Mg}_x\text{O}_2$  and  $\text{CuRh}_{1-x}\text{Mg}_x\text{O}_2$  are reviewed in Section 2. The properties of metallic delafossites are reviewed in Section 3. In Section 4 we present the theoretical analysis of metallic and thermoelectric delafossites that make up the main body of this review. Conclusions and perspectives are presented in Section 5.

## 2. Thermoelectric delafossites: doped $\text{CuCrO}_2$ and $\text{CuRhO}_2$

Many delafossites behave as semiconductors, with a band gap of order 1 eV, and have been investigated in detail for possible applications in the field of transparent conducting oxides (TCO) [19]. The delafossite family consists in a large number of materials  $\text{AMO}_2$ , with  $A = \text{Ag}^+, \text{Cu}^+ \dots$  and  $M = \text{Al}, \text{Ga}, \text{Sc}, \text{In}, \text{Fe}, \text{Cr}, \text{Rh} \dots$ . In this part, we present the results that have motivated our investigation of delafossite electronic structure and their transport properties. We focus on the results related to the doping of  $\text{CuCrO}_2$  and  $\text{CuRhO}_2$ , by substituting  $\text{Cr}^{3+}$  or  $\text{Rh}^{3+}$  by another cation such as  $\text{Mg}^{2+}$ , to increase electrical conductivity in order to optimize the thermoelectric properties, as shown in Fig. 2. The positive Seebeck coefficient for both pristine delafossites indicates their p-type character and the aliovalent substitution creating more holes in the 3d or 4d bands explains why  $S$  and  $\rho$  decrease with  $x$ . The properties of metallic delafossites with  $d^9$  A atom ( $\text{PdCoO}_2$ ,  $\text{PtCoO}_2$ ,  $\text{PdCrO}_2$  and  $\text{PtCrO}_2$ ) are described in Section 3. In contrast,  $\text{CuCrO}_2$  is semiconducting, with a magnetic transition observed at  $T_N = 24\text{ K}$  towards an antiferromagnetic state. The ratio between  $\Theta_p$  and  $T_N$  is very large, close to 7-8 suggesting a large magnetic frustration [27–29]. The possible reduction of the gap by doping has stimulated the investigation of transport properties, and more specifically and more recently, due to the  $\text{CdI}_2$  type nature of the  $\text{CrO}_2$  layers, isostructural to  $\text{CoO}_2$  layers in  $\text{Na}_x\text{CoO}_2$ , thermoelectric properties

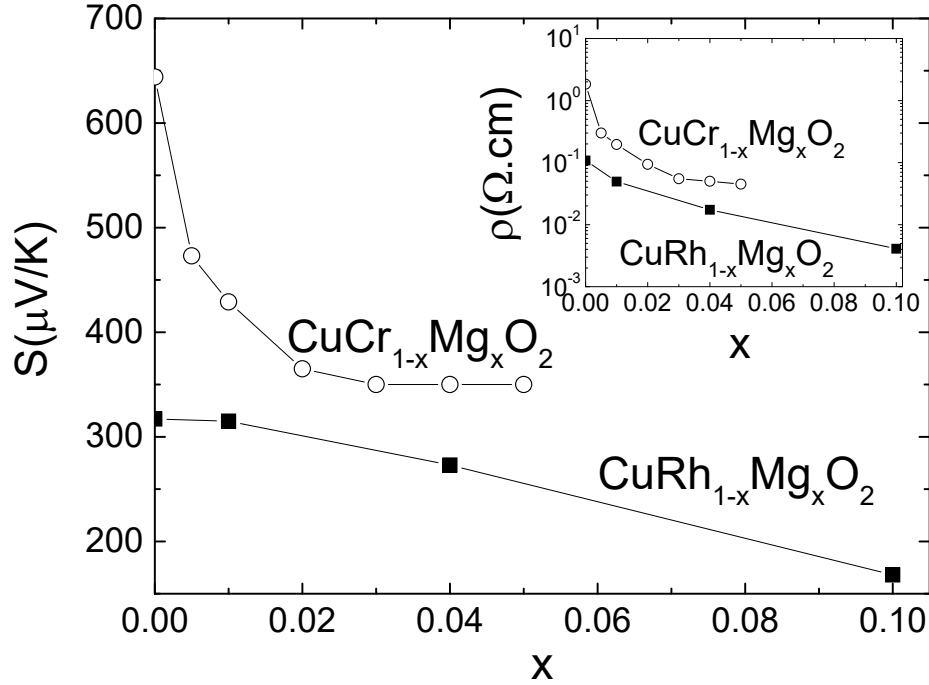


**Figure 2.** Dependence on Mg content  $x$  of the thermopower at 300 K of  $\text{CuCr}_{1-x}\text{Mg}_x\text{O}_2$  and  $\text{CuRh}_{1-x}\text{Mg}_x\text{O}_2$ . Inset: Dependence on Mg content  $x$  of the resistivity at 300 K of  $\text{CuCr}_{1-x}\text{Mg}_x\text{O}_2$  and  $\text{CuRh}_{1-x}\text{Mg}_x\text{O}_2$ .

have been measured. In 2005, a first report was presented on  $\text{CuCr}_{1-x}\text{Mg}_x\text{O}_2$  [30], probed by specific heat, magnetization and transport measurements up to 300 K. By substituting  $\text{Mg}^{2+}$  on the  $\text{Cr}^{3+}$  site, the Néel temperature  $T_N$  is kept unchanged as shown by a neutron diffraction study [28], but the Curie-Weiss temperature  $\Theta_p$  increases from  $-170$  K to  $-100$  K. Considering that  $\text{Cr}^{4+}$  is very difficult to stabilize without high oxygen pressure, the doping effect in this article was interpreted taking into account a mixed valency of  $\text{Cu}^+ / \text{Cu}^{2+}$  induced by the  $\text{Mg}^{2+}$  substitution on the  $\text{Cr}^{3+}$  site. Magnetic susceptibility was analyzed taking into account the contribution of both  $\text{Cr}^{3+}$  ( $S = 3/2$ ) and  $\text{Cu}^{2+}$  ( $S = 1/2$ ).

There is a direct impact of the antiferromagnetic ordering on the resistivity curves, with an enhanced magnetoresistance around  $T_N$  [30]. The transport results (magnetoresistance and resistivity) are consistent with a direct coupling between the doped holes and the  $\text{Cr}^{3+}$  spin. The thermopower remains rather large (still  $\sim 100 \mu\text{V/K}$  for  $x = 0.02$ ), with values close to the ones of  $\text{Na}_x\text{CoO}_2$ , but resistivity is actually too high to ensure a large power factor. The authors thus concluded that these delafossites could not be considered for thermoelectric applications.

High-temperature properties were investigated by Ono *et al.* [31], with electrical resistivity, Seebeck coefficient and thermal conductivity measured up to 1100 K and for  $x \leq 0.05$ . In this paper, contrary to the interpretation of Okuda *et al.* [30], the authors argue that a mixed valency of  $\text{Cr}^{3+}$  and  $\text{Cr}^{4+}$  is induced by the  $\text{Mg}^{2+}$  substitution on the Cr site. The Seebeck coefficient dependence on  $x$  could indeed be interpreted considering the Koshibae and Maekawa formula [32]. The  $\text{Cr}^{3+}$  and  $\text{Cr}^{4+}$  are supposed to be in the high-spin state ( $S = 3/2$  and  $S = 1$  respectively), and an extra spin entropy term of  $69.9 \mu\text{V K}^{-1}$  has to be considered. The major contribution to  $S$  nevertheless originates from the doping by itself, this term being very large due to the very small

value of  $x$ . As the resistivity remains rather large at high  $T$ , the  $ZT$  values only increase up to 0.04 for  $x = 0.03$ . The thermal conductivity is another drawback for large  $ZT$ , with  $\kappa$  between 4 and  $8 \text{ W K}^{-1}\text{m}^{-1}$  at 1000 K. Even if  $\text{CuCrO}_2$  doped delafossites exhibit modest values of  $ZT$ , larger  $ZT$  values have been obtained in  $\text{CuRh}_{0.9}\text{Mg}_{0.1}\text{O}_2$  and  $\text{CuFe}_{0.99}\text{Ni}_{0.01}\text{O}_2$  [33,34], with a maximum of 0.15 at 1000 K and 0.14 at 1100 K respectively. In  $\text{CuRh}_{0.9}\text{Mg}_{0.1}\text{O}_2$ , a smaller thermal conductivity ( $\simeq 1 \text{ W K}^{-1}\text{m}^{-1}$  at high  $T$ ), leads to this substantial enhancement of  $ZT$  with respect to doped  $\text{CuCrO}_2$  [33].

Large differences in the  $ZT$  values are thus observed between  $\text{CuCrO}_2$  and these doped  $\text{CuRhO}_2$  and  $\text{CuFeO}_2$ , and the role of  $\text{Mg}^{2+}$  on doping in  $\text{CuCrO}_2$  was still unclear. Understanding these differences [30,31] has motivated the reinvestigation of transport properties in  $\text{CuCrO}_2$  and  $\text{CuRhO}_2$  doped with  $\text{Mg}^{2+}$  [35–37]. X-ray diffraction combined with EDX analysis with transmission electron microscopy has confirmed that the solubility of  $\text{Mg}^{2+}$  is in fact very restricted ( $x \simeq 0.10$  for  $\text{CuRhO}_2$  and  $x \simeq 0.03$  for  $\text{CuCrO}_2$ ). In  $\text{CuCrO}_2$ , the substitution by  $\text{Mg}^{2+}$  rapidly leads to the formation of  $\text{CuO}$  (observed from  $x = 0.04$ ), and to the formation of the spinel  $\text{MgCr}_2\text{O}_4$  as soon as  $x = 0.01$  [37]. The evolution of the Seebeck coefficient as a function of  $x$  shows that doping is induced with the  $\text{Mg}^{2+}$  substitution even above  $x = 0.01$  (formation of the spinel  $\text{MgCr}_2\text{O}_4$ ) but is suppressed for  $x > 0.04$  as  $S$  becomes constant. The transport properties have thus been investigated up to 0.04.

The magnetic structure is not strongly affected by the  $\text{Mg}^{2+}$  substitution, as revealed by neutron diffraction [28]. From magnetic susceptibility, the high-spin state for  $\text{Cr}^{3+}$  is confirmed and large Curie-Weiss temperatures ( $-170 \text{ K}$ ) compared to a  $T_N$  of  $24 \text{ K}$  (weakly affected by  $\text{Mg}$  substitution) demonstrate the strong magnetic frustration associated to their incommensurate antiferromagnetic structure. In the entire doping range, electrical resistivity exhibits a localized behavior with  $\frac{d\rho}{dT} < 0$ , and large values of  $\rho$  close to  $10^{-1} - 10^2 \Omega \text{ cm}$  at  $300 \text{ K}$  depending on doping.  $\text{Mg}^{2+}$  substitution leads to a reduction of  $\rho$ , see the inset of Fig. 2, and for larger  $\text{Mg}^{2+}$  content,  $\rho$  can be measured down to low  $T$ , with the magnetic transition directly observed at  $24 \text{ K}$  in the  $\rho(T)$  curves. The Seebeck coefficient is positive, and evolves from a localized behavior for  $x = 0$  ( $S \propto 1/T$ , with very large values at room temperature close to  $650 \mu\text{V K}^{-1}$ , see Fig. 2) to smaller values for  $x > 0$ , with  $\frac{dS}{dT} > 0$ .

In the antiferromagnetic state, the resistivity and thermopower depend strongly on the magnetic field, as shown by the magnetothermopower and magnetoresistance curves measured up to  $9 \text{ T}$ . As discussed earlier, the introduction of  $\text{Mg}^{2+}$  could both generate a mixed valency of  $\text{Cr}^{3+}/\text{Cr}^{4+}$  or  $\text{Cu}^+/\text{Cu}^{2+}$ . The Heikes formula which was used to interpret the  $S(x)$  dependence can not discriminate between these two different doping origins. However, this existence of magnetoresistance and magnetothermopower supports the  $\text{Cr}^{3+}/\text{Cr}^{4+}$  doping, with the transport being dominated by the  $\text{Cr} - \text{O}$  network rather than the  $\text{Cu}$  network.

At higher  $T$ , for  $x > 0$ ,  $S$  continuously increases up to  $1100 \text{ K}$ , while  $\rho$  continuously decreases, leading to power factor values close to  $2 \cdot 10^{-4} \text{ W m}^{-1}\text{K}^{-2}$  [38]. This is very close to the values previously reported [31]. More discussion about the  $S(T)$  curves in connection to the band structure can be found in the Section 4.5.

In the case of  $\text{CuRhO}_2$ ,  $\text{Mg}^{2+}$  substitution can reach 10%, a value much larger than the one observed in the case of  $\text{CuCrO}_2$ .  $\text{Cu}_2\text{MgO}_3$  appears as an impurity for  $x > 0.10$ . From band structure calculations, the  $\text{Cu}$  valency has been assigned to  $\text{Cu}^+$ , while  $\text{Rh}$  is  $\text{Rh}^{3+}$  in the low spin state. With  $\text{Mg}^{2+}$  doping, the semiconducting behavior of  $\text{CuRhO}_2$  is gradually replaced by a metallic behavior, for  $T > 100 \text{ K}$  in all samples. A minimum of resistivity is observed at  $T_{\min}$ , even for  $x = 0.10$ , with  $T_{\min}$

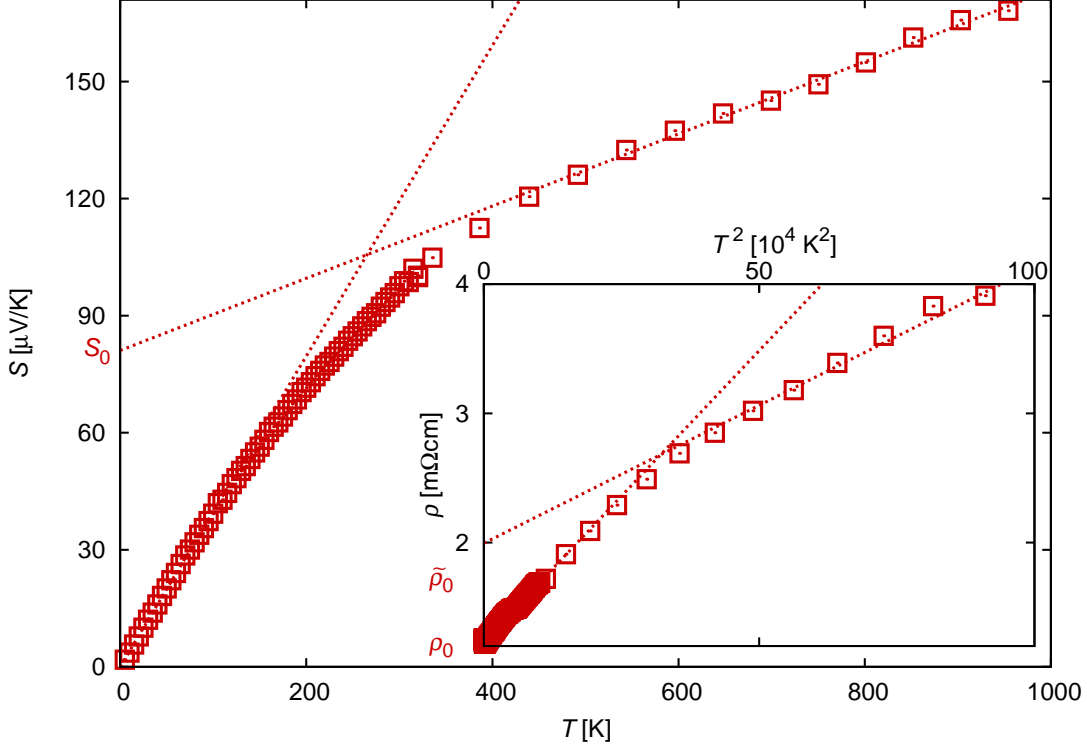


**Figure 3.** Thermopower  $S$  and resistivity  $\rho$  (inset) of  $\text{CuRh}_{0.9}\text{Mg}_{0.1}\text{O}_2$  as functions of the temperature  $T$  (squares). The linear, respectively quadratic, regions are highlighted by the dotted lines in order to show the transition from a behavior, which can be explained within a Fermi liquid picture, towards a behavior which is referred to as the one of an apparent Fermi liquid (AFL) and characterized by the additional offsets  $S_0$  and  $\tilde{\rho}_0$ .

decreasing as  $x$  increases. For large  $x$ , the resistivity values reach the  $\text{m}\Omega\text{cm}$  values, typical of the so-called ‘bad metallic’ oxides. Simultaneously, as shown in Fig. 2, the thermopower decreases from large values ( $325 \mu\text{V K}^{-1}$  for  $x = 0$ ), to values close to  $170 \mu\text{V K}^{-1}$  for  $x = 0.10$ . It must be emphasized that the Seebeck values for undoped  $\text{CuCrO}_2$  are much larger than the ones of  $\text{CuRhO}_2$ . For the latter, the spin entropy term contributing to only  $\sim 70 \mu\text{V K}^{-1}$ , the larger  $S$  difference can be ascribed to a higher self-doping in  $\text{CuRhO}_2$  naturally resulting from a small off-stoichiometry. The interesting point is that the power factor  $\frac{S^2}{\rho}$  presents a peculiar  $T$  dependence, with an almost constant value from 300 to 1000 K for  $x = 0.10$ , reaching  $6 \cdot 10^{-4} \text{ W m}^{-1} \text{ K}^{-2}$ , a value typical of the best thermoelectric oxides [37]. This peculiar behavior comes from the  $T^2$  behavior observed for the electrical resistivity in a large  $T$  range, associated to an almost  $T$  linear behavior for  $S$ . The  $S \propto T$  and  $\rho \propto T^2$  behaviors (see Fig. 3) have stimulated the development of the Apparent Fermi Liquid model [39].

Another proposed origin of the enhanced Seebeck values in Mg-doped  $\text{CuRhO}_2$  is an electronic band structure consisting of a large flat region and a sharply dispersing edge [103], a so-called ‘pudding-mold’ model. When the Fermi level is close to the transition between these two regions, the asymmetry can cause an enhanced Seebeck coefficient within the approximations of semiclassical transport.

All the above examples point out the rich variety of properties exhibited by this family of 2D materials. In this  $\text{ABO}_2$  delafossite class of compounds the pronounced two-dimensionality goes along with the triangular arrangement of transition-metal ions with rather well localized electrons, which has laid ground for the known variety



of extraordinary phenomena. In particular, when the B cation is a paramagnetic 3d metal, though there exists geometric frustration in the antiferromagnetic exchange interactions, the magnetic coupling through the separating A layer is sufficient to allow a setting of a 3D antiferromagnetic ordering as in  $\text{CuCrO}_2$  (or  $\text{PdCrO}_2$ ). The competition between the different in- and out-of-plane magnetic interactions is responsible for very different antiferromagnetic structures, collinear in  $\text{CuFeO}_2$  or non collinear in  $\text{CuCrO}_2$ . In that respect, it is very difficult to predict their spin driven multiferoic properties, ferroelectricity being spontaneous at  $T_N$  for  $\text{CuCrO}_2$  but requiring the application of a magnetic field to be induced in  $\text{CuFeO}_2$  [40]. For these antiferromagnetic insulating delafossites with  $\text{B}^{3+}$  cations, doping is necessary to induce more electronic conducting states as the  $\text{Mg}^{2+}$  for  $\text{Cr}^{3+}$  substitution in  $\text{CuCrO}_2$ , with little effect on  $T_N$ . This behavior contrasts to that of  $\text{CuRhO}_2$  with its fully occupied Rh  $4d\ t_{2g}$  ( $S = 0$ ) subshell which neither displays strong localization effects nor magnetic order but serves as a possible thermoelectric material as it combines low electrical resistivity and large Seebeck values. Finally, when the A cation is Pd or Pt as in  $\text{PdCoO}_2$  and  $\text{PtCoO}_2$  (see Section 3), very different electrical properties are observed, the samples behaving as “2D metals” characterized by extreme anisotropy creating a unique situation among all oxides. We point out that these five compounds serve only as paradigmatic examples of the whole class of delafossites and the present survey is far from being exhaustive. Indeed, the richness of phenomena can be further increased by alloying and doping.

### 3. Metallic delafossites

#### 3.1. Introduction

The majority of delafossite materials so far synthesized are semiconductors, of particular interest for their potential use as p-type transparent oxides. There is, however, a small group of materials that behave quite differently.

When the B site is occupied by Co, Rh or Cr, the  $\text{BO}_2$  layers have an electronic configuration that makes them charged but formally insulating. The octahedral crystal field around the B-site generates the familiar  $t_{2g}$  and  $e_g$  bands, and the  $t_{2g}$  bands are either completely filled by low-spin  $d^6\ \text{Co}^{3+}$  or  $\text{Rh}^{3+}$ , or effectively so by magnetic high-spin  $d^3\ \text{Cr}^{3+}$ . The resulting net single negative charge per formula unit requires that the A-site ion carry a single positive charge.

If  $\text{A}=\text{Ag}^+$  or  $\text{Cu}^+$ , the resulting electronic structure is typically gapped, despite the fact that the Ag-Ag or Cu-Cu distance can be shorter than in bulk Ag or Cu. On the other hand, the  $d^9$  configurations of  $\text{Pd}^+$  and  $\text{Pt}^+$  produce materials with extremely high, strongly anisotropic conductivity. Conduction in the triangular A-plane is mediated by close overlap between adjacent A-ions, which are separated by distances of 2.830 Å, 2.923 Å, and 3.021 Å for  $\text{Pd}(\text{Co,Cr,Rh})\text{O}_2$  [16]. This compares to a nearest neighbor distance of 2.751 Å in fcc palladium. Likewise in  $\text{PtCoO}_2$ , the interatomic distance is 2.823 Å [41], compared to 2.775 Å in the metal. For comparison, the room temperature in-plane resistivities of  $\text{PdCoO}_2$  and  $\text{PtCoO}_2$  are  $2.6\ \mu\Omega\text{ cm}$  [43] and  $2.1\ \mu\Omega\text{ cm}$  [41], much lower than for the fcc metals, which both have around  $10.6\ \mu\Omega\text{ cm}$ . This dramatic reduction in resistivity for weaker overlap is counterintuitive.

Transport out-of-plane remains metallic in character, even though the separation between consecutive A-planes is as much as 6 Å. Thus  $\text{PdCoO}_2$ ,  $\text{PtCoO}_2$ ,  $\text{PdRhO}_2$  [42] and  $\text{PdCrO}_2$  are very good metals.  $\text{PdCrO}_2$  is additionally notable because of the

frustrated antiferromagnetic ordering at 37 K.

De Haas-van Alphen [43] as well as photoemission [44] experiments show that the low-temperature Fermi surface of  $\text{PdCoO}_2$  consists of a single electron-like warped hexagonal cylinder, while that of  $\text{PdCrO}_2$  resolves into electron- and hole-like bands that arise from magnetic reconstruction of the single sheet [45,46].

An exception to this scheme is  $\text{AgNiO}_2$ , which also retains metallic character [47]. In this case the  $d^7$   $\text{Ni}^{3+}$  sets the Fermi energy in the  $e_g$  band. As the temperature is reduced, orbital degeneracy is lifted by charge transfer between Ni sites and an ordered state arises when  $3\text{Ni}^{3+} \rightarrow \text{Ni}^{2+} + 2\text{Ni}^{3.5+}$  and metallic conduction is preserved. This contrasts with other  $\text{Ni}^{3+}$  materials where Jahn Teller distortions open a gap between the  $e_g$  levels and lead to insulating ground states.

Metallic conductivity can also be obtained in many cases by doping, but these are the only stoichiometric delafossites known to produce a metallic ground state comparable to elemental metals. By contrast, the “bad metal” nature of the thermoelectric delafossites discussed in the previous section requires electronic correlations to be taken into account. Below we focus on the transport properties of the clean Pd/Pt materials, where the strong structural anisotropy and simple electronic structure make them textbook cases of quasi two-dimensional metals and give rise to effects rarely seen in the solid state.

## 3.2. Transport properties

### 3.2.1. Resistivity

$\text{PdCoO}_2$ ,  $\text{PdCrO}_2$  and  $\text{PtCoO}_2$  are notable for their very low room temperature in-plane resistivities,  $\rho(300\text{K}) = 2.6 \mu\Omega \text{ cm}$  [43],  $10 \mu\Omega \text{ cm}$  [48] and  $2.1 \mu\Omega \text{ cm}$  respectively [41]. This applies to transport confined to the ab-plane. Transport in the inter-plane direction maintains a metallic temperature dependence, although it is typically between 300 to 1000 times more resistive in nature [43,49]. This indicates that there is still some degree of overlap between Pd/Pt planes, perhaps mediated by the  $\text{BO}_2$  layers.

The resistivity of  $\text{PdCoO}_2$  has a super-linear temperature dependence not characteristic of the usual electron-phonon scattering mechanisms (Fig. 4a). The presence of optical phonon modes with a characteristic temperature of 250K was suggested to account for this [49]. The form of the resistivity curve is similar in  $\text{PtCoO}_2$  [41].

Meanwhile in the magnetic analogue  $\text{PdCrO}_2$ , the resistivity has a sub-linear temperature dependence, and is around three times higher than in  $\text{PdCoO}_2$  [48]. This sub-linearity has been related to an extended range of magnetic scattering present related to the antiferromagnetic transition at  $T_N = 37 \text{ K}$ .

The low temperature resistivity is of particular interest. In both  $\text{PdCoO}_2$  and  $\text{PtCoO}_2$  it falls to very low values, of the order of  $0.01 \mu\Omega \text{ cm}$ . A slight upturn occurs below 20K, with a magnitude of about 5% of  $\rho_0$  in  $\text{PtCoO}_2$ . This feature is so far unexplained. There is no sign of magnetic impurities that might contribute to a Kondo effect in these materials.

In  $\text{PdCoO}_2$  the resistivity below 30 K can be fit to an exponentially activated form (notwithstanding the very small upturn) [43]. This is argued to be a consequence of the simple electronic structure. Only one band crosses the Fermi energy, and the resulting Fermi surface is a closed cylinder that does not touch the Brillouin zone boundary.



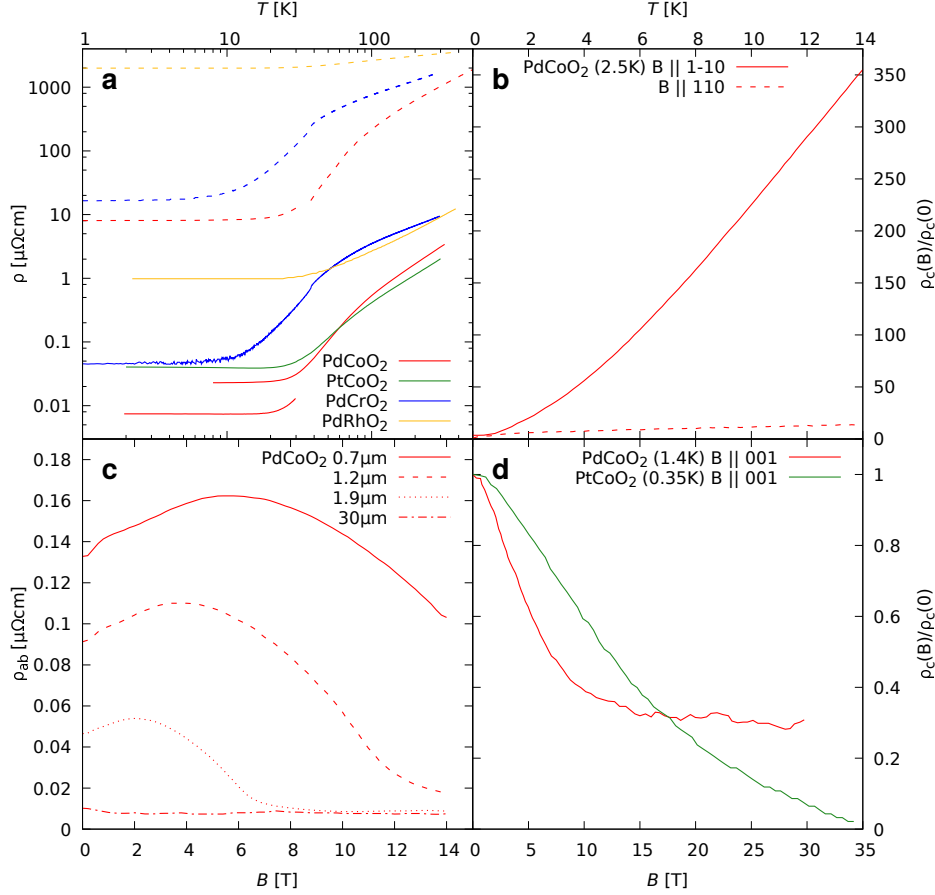


**Figure 4.** Resistivity of metallic delafossites (compiled from Refs. [41–43,49–52]). a) The solid lines show the in-plane resistivity  $\rho_{ab}$ , while the dashed lines are out-of-plane resistivity  $\rho_c$ .  $\rho_{ab}$  for two samples of PdCoO<sub>2</sub> of different residual resistivity are shown. At around 10 K both PdCoO<sub>2</sub> and PtCoO<sub>2</sub> have a shallow minimum in  $\rho_{ab}$ , and generally very similar temperature dependence and magnitude. The Néel transition in PdCrO<sub>2</sub> is seen as a small kink in both transport directions. b) Transverse magnetoresistance  $\rho_c(B)$  of PdCoO<sub>2</sub>. When the magnetic field is aligned along the  $[1\bar{1}0]$  direction, there is a huge response. c) Channel width dependence of transverse magnetoresistivity  $\rho_{ab}(B)$  in PdCoO<sub>2</sub> where the channel size is smaller than the mean free path. There is a complex dependence on magnetic field. d) Negative longitudinal magnetoresistance  $\rho_c(B)$  for PdCoO<sub>2</sub> and PtCoO<sub>2</sub>.

There is therefore a minimum phonon wavevector required for an electron-phonon umklapp scattering event to occur. Such phonons have a characteristic temperature of 30K, meaning that their population rises exponentially with this characteristic temperature. This leads to the observed exponentially activated resistivity. In the alkali metals, which also feature a single band Fermi surface entirely contained within the first Brillouin zone, the equivalent temperature is only  $\sim 4$  K.

As a consequence of this suppression of electron-phonon umklapp scattering combined with low intrinsic disorder, the mean free path can be of the order of micrometers at low temperature. The result is the observation of channel-size dependent resistivity [51] (Fig. 4c). Since umklapp scattering is one of the few mechanisms that generates resistivity in clean systems, its suppression means that the electron fluid at low temperatures has few ways to dissipate the momentum acquired under an applied electric

field. When boundary scattering becomes the dominant source of relaxation, the result is the viscous flow of electrons. It has even been suggested that if conditions are right, it may be possible to observe phenomena such as second sound in these metals at low temperatures.

The out-of-plane resistivity remains metallic (continuously increasing with temperature) for PdCoO<sub>2</sub> [49], although the exponential activation at low temperatures is not present in this direction. This is as expected, as the Fermi surface touches the zone boundary in this direction and there are no forbidden electron-phonon interactions. The super-linear behavior at high temperature is also less pronounced than for the in-plane direction.

In PdCrO<sub>2</sub>, the onset of antiferromagnetic order causes a small cusp in the resistivity as the Fermi surface reconstructs. Below  $T_N$ , the resistivity approximately follows  $T^3$ . This rapid power law arises from the suppression of scattering in the ordered state. Sub-linear temperature dependence is evident for both in- and -out-of plane resistivity [48]. Extrapolation of the magnetic susceptibility points to a Curie-Weiss temperature  $\Theta_p \sim 500$  K, an order higher than the Néel temperature. This implies a high degree of frustration. Specific heat [53] and neutron scattering [54] results point to the presence of magnetic fluctuations at temperatures between  $T_N$  and  $\Theta_p$ . Magnon-electron scattering has been proposed to explain the elevated resistivity of PdCrO<sub>2</sub> compared to non-magnetic PdCoO<sub>2</sub>.

### 3.2.2. Magnetoresistance

Strong transverse magnetoresistance (MR) is a characteristic of these materials (Fig. 4b), and becomes more pronounced at low temperatures. For in-plane current and magnetic field parallel to the c-axis, the orbital motion of quasiparticles around the cylindrical Fermi surface leads to MR of several hundred percent at low temperature. In absolute terms, however, this magnetoresistance is only of the order of a few  $\mu\Omega$  cm.

Striking results are obtained when the magnetic field is rotated in the plane and out-of-plane transport is recorded. In this case MR can be several thousand percent and depends sensitively on the in-plane field direction [55]. Six-fold patterns are observed that can be reproduced well using a semiclassical model of transport. Kohlers rule is also obeyed, implying that a single relaxation mechanism is dominant.

In the ordered state of PdCrO<sub>2</sub> the localized moments undergo a spin-flop for moderate magnetic fields applied in the plane [46]. A step is visible in the magnetoresistance curve at around 6.5 T. The same kind of spin-flop occurs at 5.3 T in semiconducting CuCrO<sub>2</sub>, where the antiferromagnetic configuration is very similar. This emphasizes the local moment nature of the magnetism; while coupling to the conduction electrons in PdCrO<sub>2</sub> is significant enough to open a gap, the magnetic ordering of the Cr<sup>3+</sup> is largely unaffected by the presence of the conduction electrons.

Negative longitudinal magnetoresistance (LMR) has been observed in PdCoO<sub>2</sub> and PtCoO<sub>2</sub> (Fig. 4d) at low temperatures and for particular field angles [52]. The occurrence of negative LMR in several materials has been taken as evidence that they belong to a class of topological materials, the Weyl semimetals. The negative LMR in those cases arises from the counterflow of surface currents in the presence of parallel electric and magnetic fields. A similar but more generic effect has been proposed that occurs in clean materials when a warped cylindrical Fermi surface undergoes Landau

quantization in strong magnetic fields [56]. Points with quasi-linear dispersion appear where the Landau tubes intersect the Fermi energy, and these play the role of the Weyl points, driving the counterflow of surface currents.

A less exotic origin of negative magnetoresistance in clean materials is the suppression of boundary scattering by strong fields when the sample dimension approaches the electronic mean free path. Cyclotron orbits smaller than the sample size can increase the distance electrons travel between collisions with the boundary, thus causing a reduction in resistance. This condition is satisfied in  $\text{PdCoO}_2$  at low temperatures for typical samples, but it is not clear if it can account for the angular dependence of the observed magnetoresistance.

### 3.2.3. Hall effect

The Hall resistivity in  $\text{PdCoO}_2$  and  $\text{PtCoO}_2$  is non-linear with magnetic field at intermediate temperatures, signaling the crossover from low- to high-field behavior [41,57]. Values of  $\omega_c\tau$  can greatly exceed unity in magnetic fields accessible in the laboratory when aligned parallel to the c-axis. The temperature dependence of the Hall coefficient is generally monotonic, reflecting the single-band electronic structure, and the values reached in the high-field limit match well with the expectation of one electron per Pd/Pt ion.

In  $\text{PdCrO}_2$ , with higher residual resistivity,  $\omega_c\tau$  reaches  $O(1)$ . A more complex temperature and magnetic field profile surrounds the Néel transition. An early report interpreted this complexity as a sign of the unconventional anomalous Hall effect [57], as there was no obvious connection between the antiferromagnetic order parameter and magnitude of the Hall coefficient. A subsequent study showed that a two-band model incorporating magnetic breakdown could reasonably account for the non-linearity of the Hall resistivity in the Néel state [45]. While the proposed breakdown fields are quite small, the antiferromagnetic gap opened in the Fermi surface is also found to be of the correct order of magnitude. A study of the temperature dependence of the Hall coefficient close to the Néel temperature revealed the impact of the short-range magnetic fluctuations on macroscopic transport [58]. Rather than being dominated by changes in diffuse scattering by magnetic excitations, the Hall coefficient smoothly interpolates between one-band and two-band electronic structures as a result of coherent scattering between hotspots by magnetic excitations. Hall effect data are shown in Fig. 5a.

### 3.2.4. Thermoelectricity

$\text{PdCoO}_2$  and  $\text{PtCoO}_2$  were suggested as interesting candidates for thermoelectric cooling on the basis of numerical calculations [59]. These showed that the c-axis Seebeck coefficient could be as large as  $-200\,\mu\text{V K}^{-1}$ , unusually large for a good metal. Combined with a limited electrical conductivity, the thermoelectric power factor  $S^2/\rho$  could be large enough for applications to become feasible.

In the planar direction, the predicted sign is positive and the magnitude is much smaller, which was in accord with an early report on polycrystalline  $\text{PdCoO}_2$  [25]. Owing to the tendency for single crystal samples to grow as thin platelets, it has

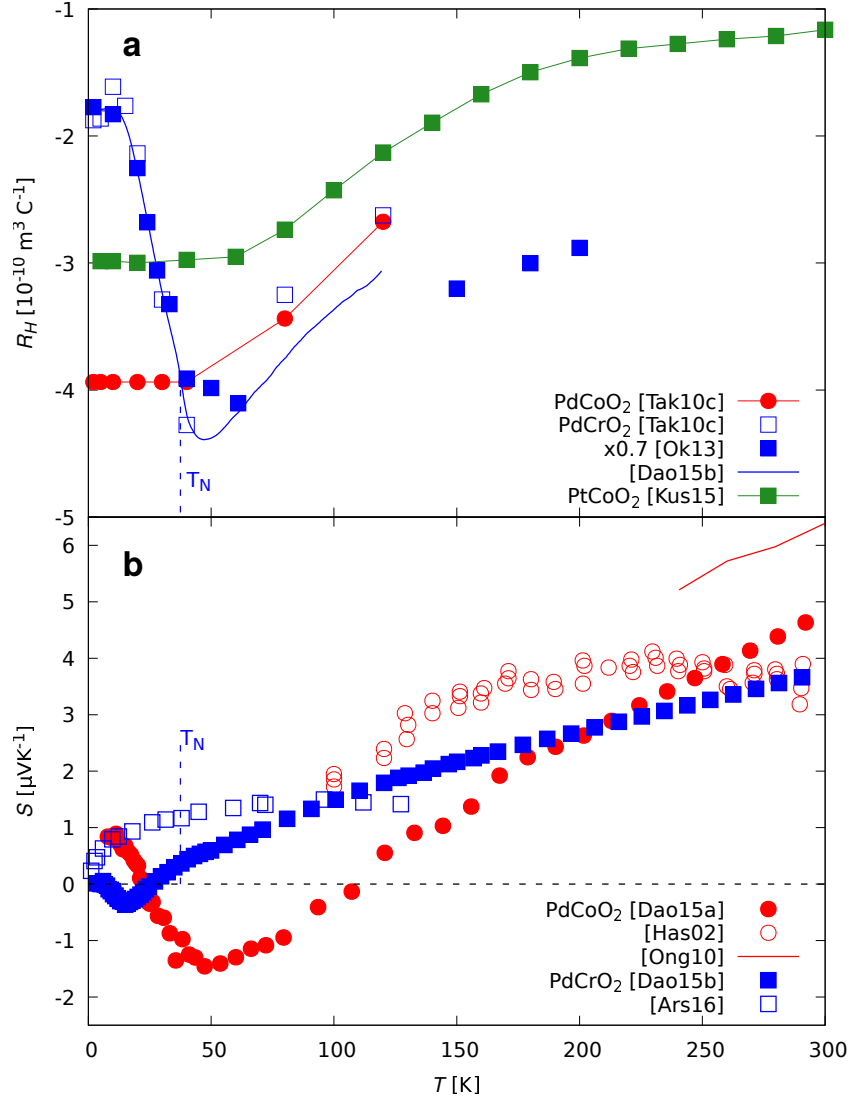


**Figure 5.** a) Hall coefficient  $R_H = \rho_{xy}/B$  of metallic delafossites in 8 T. Single band  $\text{PdCoO}_2$  [57] and  $\text{PtCoO}_2$  [41] have a temperature dependent Hall coefficient as the mean free path increases to beyond the cyclotron radius when the temperature is decreased, causing a crossover from weak-field to strong-field behavior. In contrast,  $R_H$  in  $\text{PdCrO}_2$  [45,57,58] has a complex temperature dependence due to the compensation between bands at low temperature as well as the presence of magnetic fluctuations around  $T_N$ . b) Thermoelectric power of metallic delafossites in zero magnetic field. The thermoelectric power of  $\text{PdCoO}_2$  single crystals [50] shows a phonon drag peak at low temperature and a linear dependence with temperatures at high temperatures, as expected from calculations [59]. Older polycrystalline samples [25] may have been further from stoichiometry. There are also discrepancies between results on  $\text{PdCrO}_2$  single crystals [58,61].

so far not been possible to measure the out-of-plane Seebeck coefficient, however the measured in-plane values are in good agreement with the calculations [50]. The strong predicted anisotropy and sign change of the Seebeck coefficient with respect to crystalline direction are another unique aspect of these materials. In one suggestion, this sign difference could be exploited in a monolithic type of thermoelectric device [60]. Zero-field data for  $\text{PdCoO}_2$  and  $\text{PdCrO}_2$  are shown in Fig. 5b.

The temperature dependence of the in-plane Seebeck coefficient of  $\text{PdCoO}_2$  is dom-

inated by a linear component, as expected for a good metal. The slope of this component is close to the prediction of free-electron theory [59], around  $0.018 \mu\text{V K}^{-2}$ . At low temperature there is a pronounced negative peak.

This negative peak must be ascribed to phonon drag, whereby the flow of phonons along the thermal gradient exerts an additional pressure on the electrons. This effect is most pronounced at some fraction of the Debye temperature. The presence of phonon drag was confirmed by a study of the impact of sample purity on the size of the peak: cleaner samples yield a larger drag peak [50].

In the case of  $\text{PdCrO}_2$  the experimental situation is not yet clear; two recent studies produce rather different results for the temperature dependence of the Seebeck coefficient. Ref. [58] shows a Seebeck coefficient dominated by a linear term with a weak negative peak at low temperature, much like  $\text{PdCoO}_2$ . The slope of the linear term is similar to that obtained in  $\text{PdCoO}_2$ , as expected because of the similarities in electronic structure. The low temperature peak may arise from phonon drag or from a multi-band scenario as was used to explain the Hall effect data. In magnetic fields up to 8 T, the negative peak becomes more pronounced, which argues in favor of the multi-band scenario.

However, Ref. [61] reports a Seebeck coefficient with a rather different temperature dependence. It also shows a strong suppression under intense magnetic fields, which is not seen in the moderate applied fields used in Ref. [58]. The non-linear form of the zero-field temperature dependence is somewhat unexpected, given the linear behavior in  $\text{PdCoO}_2$ , whose electronic structure should be very similar at high temperatures. The suppression of magnon drag with increasing magnetic field was invoked to explain the strong magnetic field dependence. It is difficult to reconcile the greatly different data reported in these two studies; both crystals appear to be of similar quality and exhibit the same Néel transition.

### 3.2.5. *Thermal conductivity*

The anisotropy of the thermal conductivity of  $\text{PdCoO}_2$  was extracted from a Montgomery-type experiment [50]. The results ruled out any possible application in energy conversion; the thermoelectric efficiency would be negligible because of a significant out-of-plane lattice thermal conductivity of around  $50 \text{ W K}^{-1}\text{m}^{-1}$  at room temperature. The in-plane thermal conductivity is dominated by the electronic contribution and reaches  $\sim 300 \text{ W K}^{-1}\text{m}^{-1}$  at 300 K, but with a Lorenz ratio approaching 1.1. This suggests that the lattice contribution to the thermal conductivity is much more significant than in the noble metals, for example, where the Lorenz ratio does not usually rise above unity.

### 3.2.6. *Nernst effect*

The Nernst effect was studied across the antiferromagnetic transition in  $\text{PdCrO}_2$  [58]. The Nernst effect is the thermoelectric equivalent of the Hall effect and is sensitive to changes in mobility and carrier number. In  $\text{PdCrO}_2$ , the Nernst coefficient also responds to the presence of the antiferromagnetic fluctuations that foreshadow long-range order. The response can be understood within the same framework as the Hall

effect, where the opening of the gaps at the hotspots is smoothed by the presence of fluctuations. In the ordered, two-band state the Nernst coefficient is large and depends strongly on magnetic field, while in the paramagnetic single-band phase it is small and of a magnitude compatible with a high carrier density. The crossover region is characterized by a sign change and a strong increase in magnitude.

### 3.2.7. Discussion

The simplicity of the electronic structure in  $\text{PdCoO}_2$  and  $\text{PtCoO}_2$  leads to interesting transport properties even in the absence of strong correlations. These materials are self-organising on the nanoscale, alternating conducting and insulating layers. In the case of  $\text{PdCrO}_2$ , the insulating layer also supports local moment magnetism. This unique material permits the study of symmetry breaking on transport properties without contaminating the conduction layer with magnetic ions.

## 4. Theoretical analysis

### 4.1. Electronic structure

Since its invention about five decades ago, density functional theory has witnessed a tremendous success story in predicting, explaining, and understanding the electronic properties of matter. This overwhelming progress was initiated by the fundamental work of Hohenberg, Kohn, and Sham, who established the electronic density as the key variable to access the properties of the ground state [62,63]. Nowadays, density functional theory is an integral and indispensable part of condensed matter research and materials science, which impressively complements experimental studies and has found its way into industrial laboratories [64,65].

Since calculations as based on density functional theory, usually called first principles calculations, do not need any input data other than the atomic numbers of the constituent atoms and their initial coordinates, they serve as an ideal and independent starting point for any investigation of materials. While summarizing recent first principles work, we largely follow the discussion presented in previous publications by our group, which should be consulted for a detailed account of all results [35,37,66,67]. In the present context we mention only that all calculations were performed using the augmented spherical wave (ASW) method, which likewise is described in some detail elsewhere [68,69].

### 4.2. $\text{PdCoO}_2$ and $\text{PtCoO}_2$

A number of electronic structure investigations of these two Co-delafoossites have been reported in the literature. Most of them focused on the extraordinary conductivity and specifically tried to clarify the composition of the wave functions at the Fermi energy. In particular, linear muffin-tin orbital calculations were performed by Seshadri *et al.* as well as by Okabe *et al.* [70,71]. The former authors, who also investigated  $\text{PtCoO}_2$ , attributed the density of states at  $E_F$  mainly to the Pd 4d states with only small contributions from the Co 3d and O 2p orbitals. In contrast, photoemission data were interpreted assuming the density of states at the Fermi energy arises exclusively



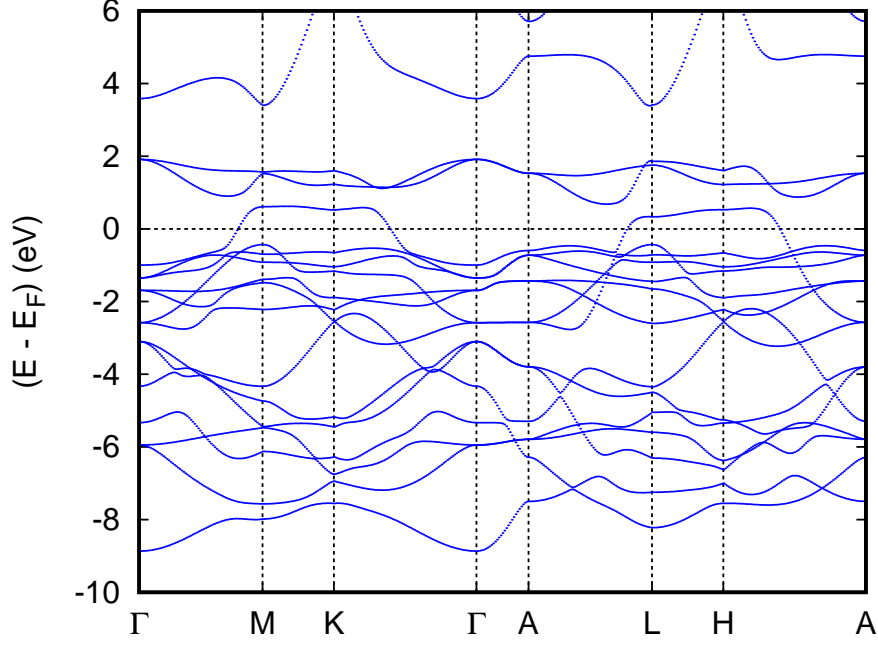


**Figure 6.** Electronic bands of PdCoO<sub>2</sub>. Reprinted with permission from (Chem. Mater. **20**, 2370 (2008)). Copyright (2008) American Chemical Society.

from the Pd 4*d* states [17,18,72]. Furthermore, from the combination of photoemission spectroscopy and inverse photoemission spectroscopy it was concluded that the Fermi energy is located in a shallow minimum of the density of states and doping may thus cause rather high values of the thermoelectric power [25,72,73]. Hence, an investigation as that described below was needed to resolve the controversy by identifying the influence of the different atomic species and orbitals on the electronic properties and thereby to make closer connection with the photoemission data [66]. In contrast to previous calculations in the literature, which were based on the crystal structure data by Shannon, Rogers, and Prewitt [16], fully optimized lattice parameters and atomic positions as given in Table 1 were used.

In discussing the electronic properties of the two cobaltates we start displaying the electronic bands along high-symmetry lines of the first Brillouin zone of the hexagonal lattice as well as the partial densities of states (DOS) in Figs. 6 and 7, respectively. The somewhat complicated structure of both the electronic bands and the DOS results from the energetical overlap of the relevant orbitals in the energy interval shown. Yet, close to the Fermi energy this complexity clears up completely and only a single band straddles  $E_F$ , leading to a very simple Fermi surface. Since a detailed discussion of the results can be found in Ref. [66], we here focus on the most important findings. These

**Table 1.** Experimental and calculated lattice parameters (in Å) and atomic positions.

compound		a	c	$z_O$
PdCoO <sub>2</sub>	exp.	2.8300	17.743	0.1112
	calc.	2.8767	17.7019	0.1100
PtCoO <sub>2</sub>	exp.	2.8300	17.837	0.1140
	calc.	2.8989	17.458	0.1128

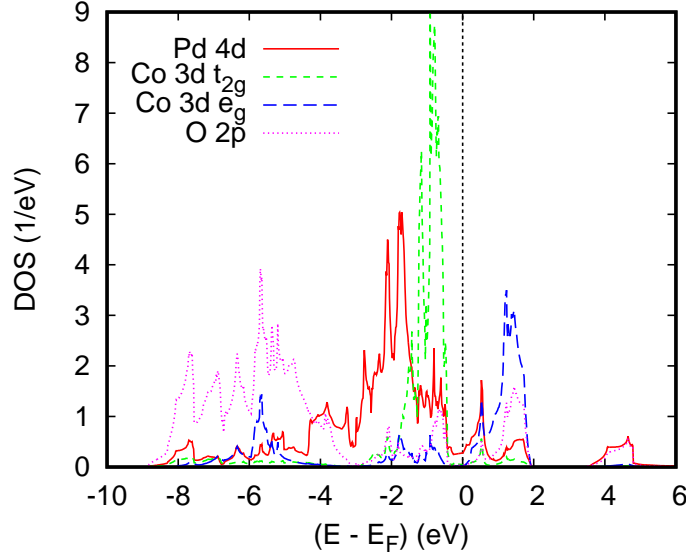


**Figure 7.** Partial densities of states (DOS) of PdCoO<sub>2</sub>. Selection of Co 3d orbitals is relative to the local rotated reference frame, see text. Reprinted with permission from (Chem. Mater. **20**, 2370 (2008)). Copyright (2008) American Chemical Society.

include the crossover from predominant O 2p bands to a set of sharp peaks due to transition metal *d* states at about  $-4$  eV and a clear separation of the Co 3d states into their  $t_{2g}$  and  $e_g$  manifolds due to the octahedral coordination by oxygen atoms. Note that the latter observation refers to a local rotated coordinate system with the Cartesian axes pointing approximately towards the oxygen atoms. Since the Fermi energy falls right between the  $t_{2g}$  and  $e_g$  manifolds, Co is found in a  $d^6$  low-spin state. In this respect PdCoO<sub>2</sub> is thus not unlike CuRhO<sub>2</sub> to be considered below. However, while in the latter compound the *d* orbitals are fully occupied and, hence, allow for the semiconducting behavior, the missing electron in PdCoO<sub>2</sub> leads to incomplete band filling and the finite conductivity. In conclusion, the above results confirm the picture of trivalent Co and monovalent Pd in a  $d^9$  configuration [16–18]. At the same time, they clearly reveal the only tiny contribution of the Co and O states to the electrical conductivity, which is carried almost exclusively by the Pd 4d states.

It is very instructive to further analyze the latter in terms of their five 4d partial DOS, which are shown in Fig. 8. Since Pd is linearly coordinated by two oxygen atoms parallel to the *c* axis and has six Pd neighbors in the *a-b* plane, to this end the global coordinate system is used. With this choice, contributions from the  $d_{xy}$  and  $d_{x^2-y^2}$  as well as from the  $d_{xz}$  and  $d_{yz}$  states are identical. The Pd 4d partial DOS are strongly influenced by the linear coordination. Again, without going into details, we mention the strong  $\sigma$ -type  $d_{3z^2-r^2}$ - $p_z$  overlap along the *c* axis as indicated by the striking similarity of the corresponding partial DOS in the energy range from  $-9$  to  $-4$  eV as well as the broad Pd  $d_{xy,x^2-y^2}$  bands reflecting the short in-plane Pd-Pd distances, which are very close to those of metallic Pd. Obviously, these latter states and the  $d_{xy,x^2-y^2}$  states add the largest contributions to the total DOS at  $E_F$ , whereas that of the  $d_{xz,yz}$  states is almost negligible. Finally, the sharp peak of the  $d_{3z^2-r^2}$  partial DOS at about  $+0.6$  eV can be clearly assigned to the almost dispersionless band along the lines M-K and L-H.

Finally, the Fermi surface shown in Fig. 9 underlines the strong quasi two-

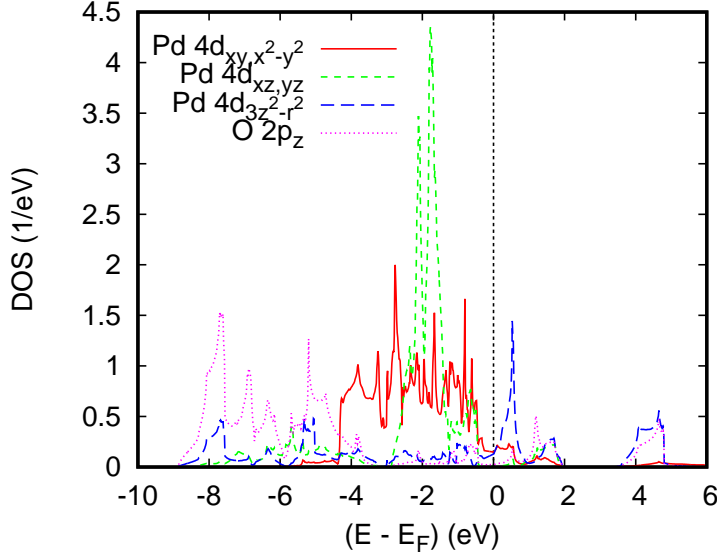


**Figure 8.** Partial Pd 4d and O 2p<sub>z</sub> DOS of PdCoO<sub>2</sub>. Reprinted with permission from (Chem. Mater. **20**, 2370 (2008)). Copyright (2008) American Chemical Society.

dimensionality of the electronic states and, hence, explains the strong anisotropy in electric conductivity.

The physical picture emerging from the above results agrees very well both with previous calculations [70,71] and more recent first-principles studies [59,74,75]. They are also in agreement with photoemission and x-ray absorption data by Tanaka *et al.*, Higuchi *et al.*, and Noh *et al.* [17,44,72,76], who likewise attribute the metallic conductivity almost exclusively to the Pd 4d states and even regard PdCoO<sub>2</sub> as a metal-insulator stack structure [44]. These authors attribute the high conductivity to the strong dispersion of the conduction band, the large Fermi surface, and the long lifetime of the charge carriers. The extraordinary transport properties of PdCoO<sub>2</sub> were studied by Takatsu *et al.*, by Ong *et al.*, by Gruner *et al.*, as well as by Daou *et al.*, who reported on the strong anisotropy of the electrical conductivity [49,50] and the thermoelectric power [59,75]. This goes along with de Haas-van Alphen measurements of Hicks *et al.*, who found anomalously low contributions from electron-phonon, electron-electron, and electron-impurity scattering to the resistivity [43]. Finally, the exceptional magnetoresistance has been discussed by Takatsu *et al.* as well as Kikugawa *et al.* [52,55].

There is a dispute about the detailed composition of the electronic wave functions at the Fermi surface. Arguments in favor of hybridized Pd  $d_{3z^2-r^2}$ -5s orbitals were supported by Kimura *et al.* [77]. However, the above results demonstrate that the metallic conductivity is maintained by the in-plane  $d_{xy}$  and  $d_{x^2-y^2}$  orbitals and the in-plane part of the  $d_{3z^2-r^2}$  orbitals to a similar degree with a somewhat greater influence of the former.

In passing, we mention very similar findings for PtCoO<sub>2</sub>. Yet, the anisotropy of the electrical conductivity is reduced in this compound due to the larger extent of the Pt 5d orbitals and the resulting increased overlap of the in-plane  $d$  states as well as with the O 2p states.

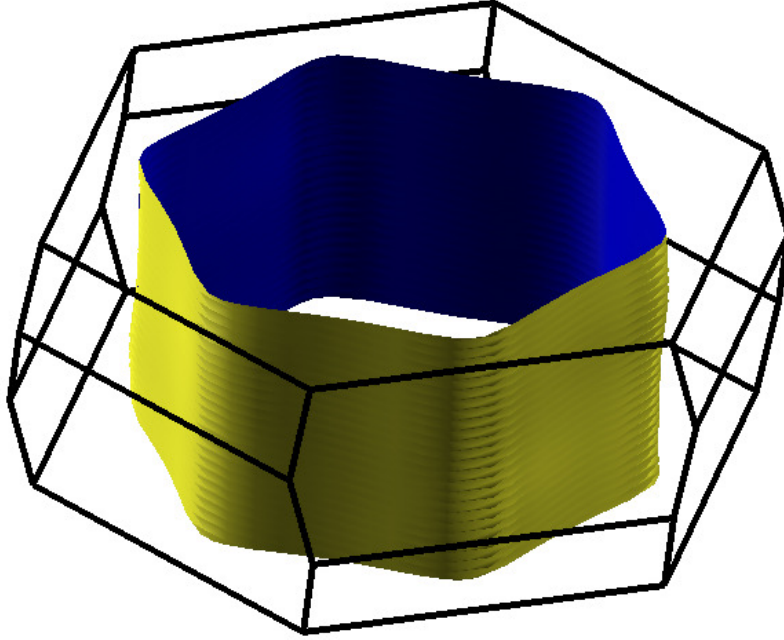


**Figure 9.** Fermi surface of PdCoO<sub>2</sub>. Reprinted with permission from (Chem. Mater. **20**, 2370 (2008)). Copyright (2008) American Chemical Society.

### 4.3. CuFeO<sub>2</sub>

As already mentioned before, one of the most attractive properties of the delafossites arises from the arrangement of transition-metal ions on a two-dimensional triangular lattice, which allows to study, *e.g.*, frustration effects, incommensurate and commensurate non-collinear magnetic order, unusual spin coupling, and multiferroic behavior. CuFeO<sub>2</sub> and CuCrO<sub>2</sub> have found much interest in this context and are therefore also considered in this overview.

The investigations of magnetic delafossite compounds has been from the very beginning accompanied by the search for distortions occurring at low temperatures in order to escape the geometric frustration. For this reason, the exact atomic and magnetic structure of many of these compounds has long been a matter of extensive dispute. This is not different for CuFeO<sub>2</sub> [27,78]. Furthermore, there has been also some dispute about the possible occurrence of multiple magnetic phase transitions. From neutron diffraction data, Mekata *et al.* identified two magnetic transition for CuFeO<sub>2</sub> at  $T_{N1} = 16$  K and  $T_{N2} = 11$  K. The magnetic phases required monoclinic and orthorhombic magnetic supercells of the undistorted rhombohedral unit cell with commensurate and incommensurate collinear arrangements of the localized  $4.4\mu_B$  Fe<sup>3+</sup> moments [79–82]. More importantly, using x-ray and neutron diffraction measurements, Ye *et al.* indeed found structural distortions below 4 K accompanying the magnetic phase transitions and leading to a monoclinic lattice with space group  $C2/m$  [83]. In addition, analysis of spin-wave spectra gave strong hints at a three-dimensional magnetic coupling [84]. It was also found that in response to a magnetic field the magnetic transition temperatures lower and an incommensurate structural distortion as well as ferroelectricity is induced [83]. Observation of a noncollinear-incommensurate phase in magnetic field was likewise taken as indicative of multiferroic behavior by Kimura

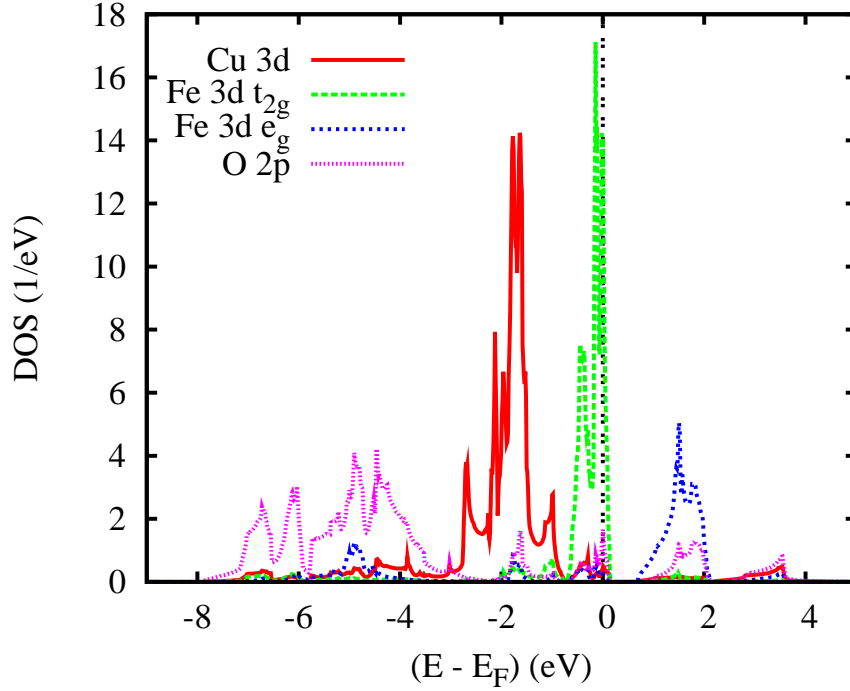


**Figure 10.** Partial densities of states (DOS) of rhombohedral  $\text{CuFeO}_2$ . Selection of Fe 3d orbitals in this and the subsequent figures is relative to the local rotated reference frame, see text. Reprinted with permission from (Phys. Rev. B **78**, 052402 (2008)). Copyright (2008) American Physical Society.

*et al.* [82] and later on indeed identified in Al-doped  $\text{CuFeO}_2$  [85]. Further indication of multiferroic behavior was taken from inelastic neutron scattering data [84]. Rut-tapanun *et al.* have pointed to the potential of Pt-doped  $\text{CuFeO}_2$  for thermoelectric applications [86].

Despite strong interest, only few electronic structure calculations for magnetic delafossite compounds had been reported [70,87–89]. This is possibly due to the still much debated atomic and magnetic structure. For that reason, only the ferromagnetic configuration was considered. Yet, the results were contradictory. Galakhov *et al.* reported on a ferromagnetic ground state for the rhombohedral  $R\bar{3}m$  structure with a magnetic moment at the Fe site of about  $0.9 \mu_B$ , much lower than the experimental value [87]. Furthermore, the Fe 3d  $t_{2g}$  states were found above the Cu 3d states just at the Fermi energy, again in disagreement with both photoemission data and the fact that  $\text{CuFeO}_2$  is a semiconductor with an optical band gap of about 1.15 eV. In contrast, LDA+ $U$  calculations revealed a band gap of 2 eV and a magnetic moment of  $3.76 \mu_B$ . However, the occupied Fe 3d states were located at about 9 eV below the valence band maximum and thus much too low [87]. More recently, Ong *et al.* found in their calculation a high-spin state with a magnetic moment of  $3.78 \mu_B$  per Fe and the Fe 3d  $t_{2g}$  spin-up states below the Cu 3d bands in agreement with photoemission and x-ray emission data [88]. However, again a finite optical band gap was arrived at only after taking into account local electronic correlations within the GGA+ $U$  scheme.

We begin a detailed analysis by discussing the density of states (DOS) arising from spin-degenerate calculations for the rhombohedral structure as displayed in Fig. 10. Crystal structure data by Ye *et al.* [83] are used throughout. As for  $\text{PdCoO}_2$ , a crossover from dominating O 2p states to a sequence of sharp transition metal  $d$  states is observed

at about  $-3$  eV. While Cu is found in a monovalent  $d^{10}$  configuration in good agreement with experiment, Fe assumes a  $d^5$  state with the Fermi energy falling into the upper part of the  $t_{2g}$  manifold. Note that in distinguishing the  $t_{2g}$  and  $e_g$  manifolds we again used the local rotated coordinate system with the Cartesian axes adjusted to an assumed perfect oxygen octahedron. Details can be found in Ref. [67].

In order to be in line with the previous work by Galakhov *et al.* as well as by Ong *et al.* [87,88], we next mention spin-polarized calculations for an assumed ferromagnetic state. Three different configurations were obtained corresponding to a low-spin, intermediate-spin, and high-spin moment located at the Fe site. The total energies as compared to the spin-degenerate configuration and the local magnetic moments are summarized in Table 2. All three ferromagnetic configurations are lower in energy than the spin-degenerate case with the high-spin state being the most stable as long as the lattice is restricted to be rhombohedral. The results thus confirm both the low-spin and high-spin calculations by Galakhov *et al.* as well as by Ong *et al.*. In particular, they assign the differences between their findings to the existence of difference spin states.

In a second step, the monoclinic structure observed by Ye *et al.* is considered [83]. Since this monoclinic unit cell still contains one Fe atom it allows only for spin-degenerate and spin-polarized ferromagnetic calculations. The resulting total energies and magnetic moments are given in Table 2. While the latter are very similar to those obtained for the rhombohedral structure, the total energies are all lower by several mRyd with the largest energy lowering occurring for the high-spin state. In passing, we mention that the similarities between the results obtained for both structures extend also to the partial densities of states.

Finally, we turn to calculations for the eightfold magnetic supercell proposed by Ye *et al.* [83]. The resulting partial DOS are displayed in Fig. 11 and the local magnetic moments and total energy included in Table 2. Obviously, the antiferromagnetic state has the lowest energy as compared to all other configurations and Fe is found to be in a high-spin state in agreement with the neutron diffraction data by Mekata *et al.* [79,80]. Moreover, the calculation yields a band gap of 0.05 eV, in contrast to all previous results for  $\text{CuFeO}_2$ . The results for the ferromagnetic high-spin states as well as the antiferromagnetic ground state have been nicely confirmed by Zhong *et al.*, who, in addition, discussed the multiferroic behavior in terms of the hybridization of the Fe  $3d$  and O  $2p$  states [90]. In order to obtain a band gap in closer agreement with experiment, Hiraga *et al.* performed GGA+ $U$  calculations and obtained a band gap of about 1 eV for  $U = 4$  eV [91].

**Table 2.** Total energies (in mRyd per formula unit) and magnetic moments (in  $\mu_B$ ) for different crystal structures and magnetic orderings of  $\text{CuFeO}_2$ .

structure	magn. order	$\Delta E$	$m_{\text{Fe}}$	$m_{\text{O}}$
rhombohedral	spin-deg.	0.0		
rhombohedral	ferro (LS)	-16.7	1.03	-0.02
rhombohedral	ferro (IS)	-12.0	2.02	-0.02
rhombohedral	ferro (HS)	-19.2	3.73	0.21
monoclinic	spin-deg.	-6.0		
monoclinic	ferro (LS)	-21.5	1.04	-0.02
monoclinic	ferro (IS)	-19.0	2.08	-0.02
monoclinic	ferro (HS)	-32.0	3.62	0.19
monoclinic	antiferro	-46.0	$\pm 3.72$	$\pm 0.08$



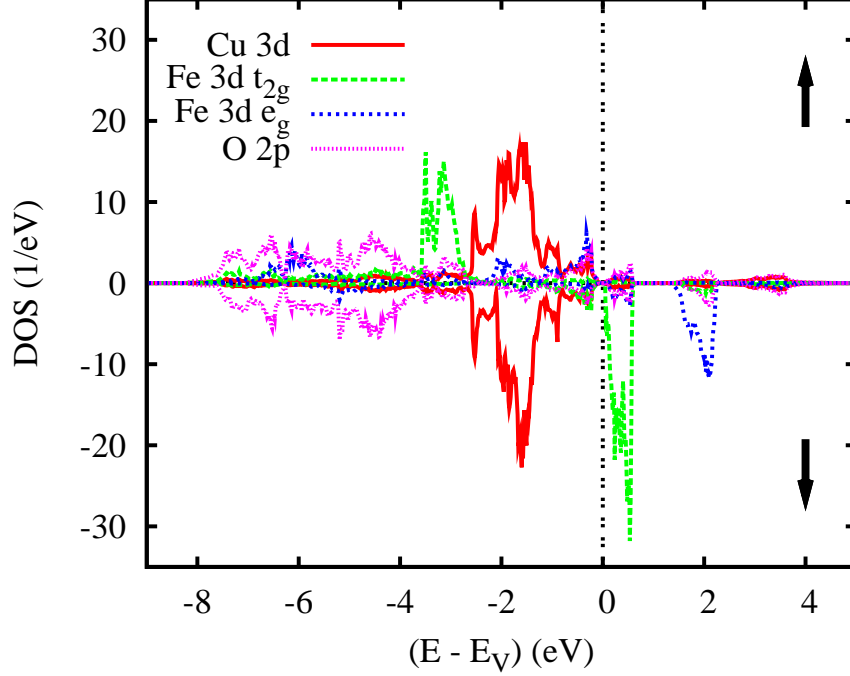


**Figure 11.** Partial densities of states (DOS) of monoclinic antiferromagnetic high-spin  $\text{CuFeO}_2$ . Reprinted with permission from (Phys. Rev. B **78**, 052402 (2008)). Copyright (2008) American Physical Society.

#### 4.4. $\text{CuCrO}_2$

$\text{CuCrO}_2$  is yet another example for strong geometric frustration effects coming with the predominantly antiferromagnetic coupling of rather well localized magnetic moments on a triangular lattice. However, unlike  $\text{CuFeO}_2$ ,  $\text{CuCrO}_2$  does not show any deformation of the atomic structure down to lowest temperatures. The magnetic structure has been at the center of controversial debates for a long time. While early neutron powder diffraction work was in favor of an out-of-plane  $120^\circ$  spin structure with a commensurate propagation vector along the  $(\frac{1}{3}, \frac{1}{3}, 0)$  direction [92], more recent studies revealed two possible structures, namely, a helicoidal and a cycloidal structure with incommensurate propagation vector  $(0.329, 0.329, 0)$  below  $T_N = 24$  K [28]. More recently, single-crystal polarized neutron diffraction found the spiral plane to be parallel to the (110) plane [93]. Building on x-ray diffraction measurements, Kimura *et al.* reported on a slight deformation of the triangular lattice plane accompanying the magnetic ordering [94]. However, this finding has not been confirmed by other groups.

According to neutron powder diffraction data, magnetic susceptibility measurements, electrical permittivity and electrical polarization data of magnetically diluted  $\text{CuCr}_{1-x}\text{M}_x\text{O}_2$  with  $\text{M} = \text{Al}, \text{Ga}, \text{Sc}, \text{Rh}$  by Pachoud *et al.* the magnetic ground state turned out to be very robust against removal of Cr [95]. These authors thus concluded that the magnetic ground state of  $\text{CuCrO}_2$  is very different from that of  $\text{CuFeO}_2$ .

In order to arrive at a better understanding of this material both spin-degenerate and spin-polarized calculations using the crystal structure data reported by Crottaz *et al.* [96] were performed. As for the other compounds discussed above, the partial densities of states as resulting from the spin-degenerate calculations have the lower part of the spectrum dominated by O 2p states, whereas the transition metal *d* states

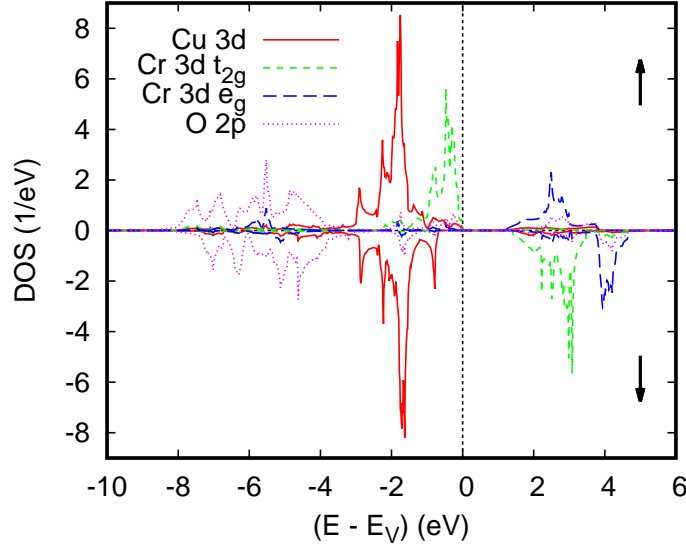


**Figure 12.** Partial densities of states (DOS) of rhombohedral ferromagnetic  $\text{CuCrO}_2$ . Reprinted from Solid State Commun. **149**, A. Maignan, C. Martin, R. Frésard, V. Eyert, E. Guilmeau, S. Hébert, M. Poienar, and D. Pelloquin, *On the strong impact of doping in the triangular antiferromagnet  $\text{CuCrO}_2$* , 962-967, Copyright (2009) with permission from Elsevier.

show rather sharp peaks above  $-4$  eV. While Cu again is found in a monovalent  $d^{10}$  configuration in close analogy with experimental findings, the Cr  $3d$  states fall into half-occupied  $t_{2g}$  and empty  $e_g$  manifolds. From the  $d^3$  configuration and the fact that  $E_F$  is very close to the highest peak one would expect long-range ferromagnetic ordering of Cr moments of  $3 \mu_B$  in a spin-polarized calculation.

In view of the complex magnetic structure observed for  $\text{CuCrO}_2$  it is useful to start spin-polarized calculations by first considering an assumed ferromagnetic order. This procedure is well motivated by the previous work on  $\text{CuFeO}_2$ , where we also started investigating an assumed ferromagnetic high-spin state before performing calculations for the antiferromagnetic ground state proposed by Ye *et al.* and found a strong similarity of the partial densities of states arising from these two configurations. Hence, we can learn a lot about the local electronic properties already from studying the ferromagnetic state.

Now, from spin-polarized calculations for an assumed ferromagnetic configuration of  $\text{CuCrO}_2$ , a stable ferromagnetic configuration was obtained with magnetic moments of  $3.0 \mu_B$ . Most importantly, the density of states as displayed in Fig. 12 reveals a fundamental band gap of about 1.2 eV between the spin-up and spin-down Cr  $3d t_{2g}$  states, which also carry the overwhelming part of the magnetic moment. Except for the lower filling of the Cr  $3d t_{2g}$  states the partial densities of states look very similar to those of  $\text{CuFeO}_2$ , which fact saves us a detailed discussion here.

The electronic bands along selected high-symmetry lines of the first Brillouin zone of the hexagonal lattice as displayed in Fig. 13 reveal substantial three-dimensional dispersion, which we attribute to the coupling between the layers. Yet, the dispersion is considerably reduced close to the valence band maximum. In addition, the highest occupied states at M and K are almost identical to those at L and H. Hence, there is almost no dispersion of these bands along the lines M-L and K-H. As a consequence, within a rigid band approximation, we would expect strongly localized bands arising

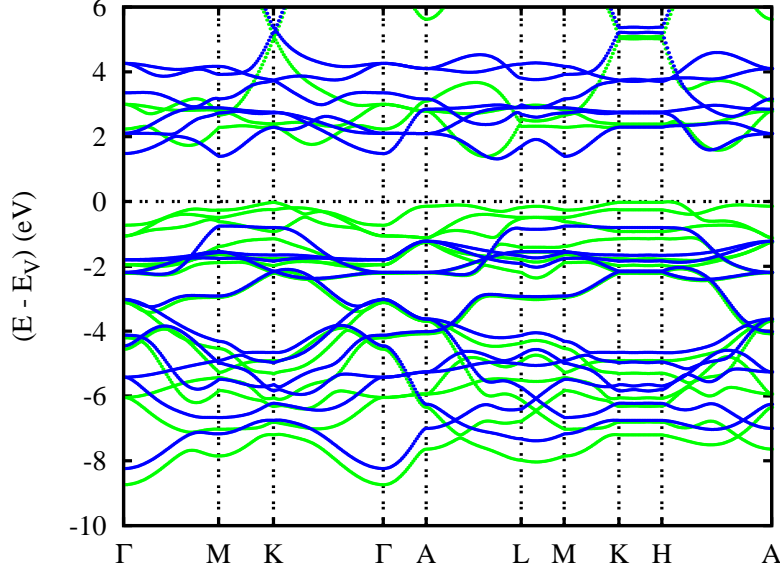


**Figure 13.** Electronic bands of rhombohedral ferromagnetic  $\text{CuCrO}_2$ . Green (blue) curves correspond to the majority (minority) spin bands. Reprinted from Solid State Commun. **149**, A. Maignan, C. Martin, R. Frésard, V. Eyert, E. Guilmeau, S. Hébert, M. Poienar, and D. Pelloquin, *On the strong impact of doping in the triangular antiferromagnet  $\text{CuCrO}_2$* , 962-967, Copyright (2009) with permission from Elsevier.

from small hole doping, which would induce finite but still small Fermi velocities driving spin-dependent transport.

Performing GGA+ $U$  calculations for a variety of delafossites, Scanlon and coworkers considered an antiferromagnetic structure for  $\text{CuCrO}_2$  with ferromagnetic alignment within the sandwich planes and antiferromagnetic alignment of neighboring planes [97–99]. In addition, hybrid functional calculations were performed. While the authors also obtained a band gap separating occupied  $d$  states from empty Cr  $3d$   $e_g$  bands of about 1, 2, and 3 eV from their GGA, GGA+ $U$ , and hybrid functional calculations, respectively, their results are at some variance with those presented above. In particular, Cu  $3d$  and Cr  $3d$   $t_{2g}$  states are both found in the same energy interval ranging from about  $-3$  eV to the valence band maximum and bands close to the latter mainly trace back to the Cu states [97–99]. A very similar order of bands was obtained by Hiraga *et al.* [91].

In order to arrive at a more complete picture, we complemented the above calculations for the assumed ferromagnetic state with calculations for the antiferromagnetic structure proposed by Scanlon and coworkers. This structure requires a hexagonal rather than rhombohedral unit cell with a doubling of the hexagonal  $c$  axis and it comprises six formula units. The resulting partial densities of states and electronic bands are display in Figs. 14 and Fig. 15. Note that while representing the electronic band structure we used the Brillouin zone of the original small cell and, hence, obtain threefold band oscillations along the line  $\Gamma$ -A. Apart from that, both the band structure and the partial densities of states are very similar to those obtained for the assumed ferromagnetic order and thus confirmed our above expectations, namely, that the electronic properties are already very well described by those for an assumed ferromagnetic state. Still, especially the spin-majority Cr  $3d$   $t_{2g}$  bands at the valence band maximum are much more localized in the antiferromagnetic configuration. Nevertheless, the discrepancy as compared to the results by Scanlon *et al.* are not yet resolved.

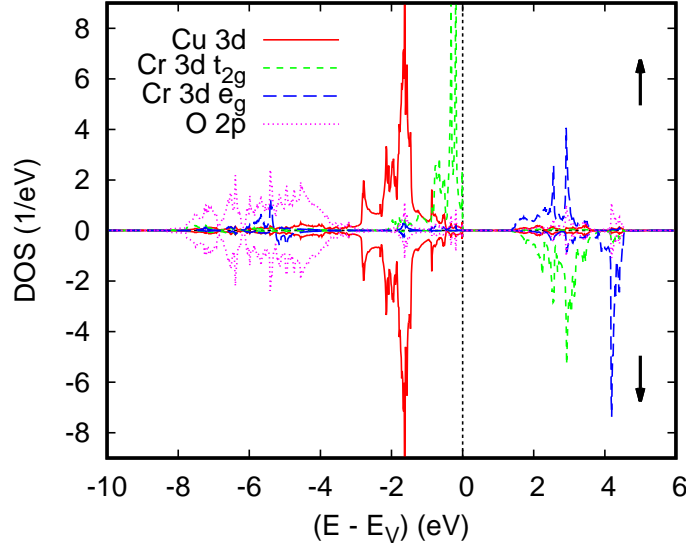


**Figure 14.** Partial densities of states (DOS) of hexagonal antiferromagnetic  $\text{CuCrO}_2$ .

As a consequence, the predominant character of the wave function occurring on small hole doping is not known.

The issue has been critically discussed from both an experimental and a theoretical point of view by Yokobori *et al.*, who combined photoemission spectroscopy, soft x-ray absorption spectroscopy, and electronic structure calculation within the LDA+ $U$  approximation as applied to the rhombohedral ferromagnetic configuration [100]. These authors confirmed the above results with the Cr  $3d t_{2g}$  dominating the valence band maximum and the fully occupied Cu  $3d$  bands found well below. Nevertheless, their x-ray absorption spectra on  $\text{CuCr}_{1-x}\text{Mg}_x\text{O}_2$  showed a strong sensitivity to the Mg content indicating the hole will be doped into the Cu sites in contradiction to their photoemission spectra. In order to resolve the issue, Yokobori *et al.* proposed strong Cu  $4s$ -Cr  $3d$  charge transfer via the O  $2p$  states. Nevertheless, this puzzling situation is still awaiting further insight.

Calculations of Jiang *et al.*, which took into account non-collinear spin arrangements, revealed predominantly in-plane exchange interactions and an incommensurate spin-spiral structure with a (110) spiral plane and a screw-rotation angle close to  $120^\circ$  in agreement with experimental data [93,101]. While spin-orbit interaction was shown to have only minor influence on the electronic properties spin frustration had a stronger effect on the  $d$ - $p$  hybridization. Finally, Monte Carlo simulations using exchange parameters extracted from supercell calculations led to a Néel temperature of 29.9 K, again in acceptable agreement with the experimental findings [101]. Recent Monte Carlo simulations taking small lattice distortions into account yield a Néel temperature of  $T_N \simeq 27 \text{ K}$ . Furthermore, a connection between the emergence of spin helicity below  $T_N$  and ferroelectricity could be established [29].

#### 4.5. $\text{CuRhO}_2$

Finally, we turn to yet another delafossite compound, which has recently attracted much interest from a completely different perspective, namely, as a very promising

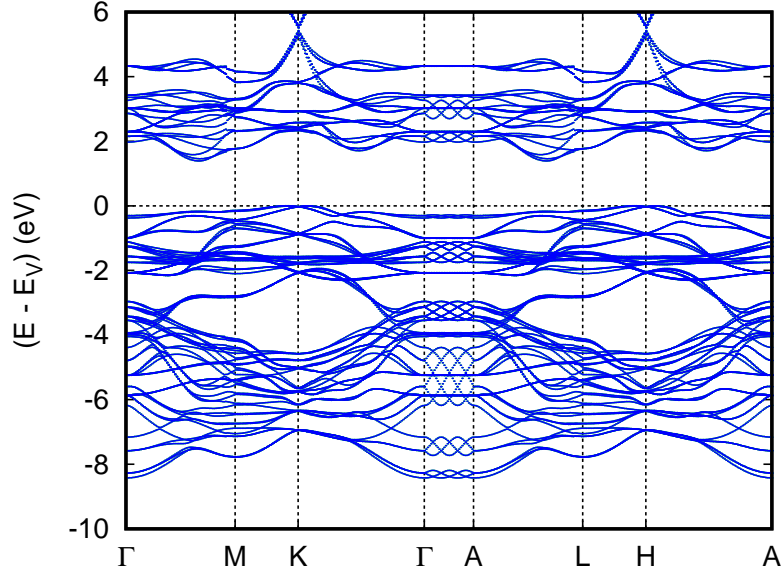


**Figure 15.** Electronic bands of hexagonal antiferromagnetic  $\text{CuCrO}_2$ .

candidate for applications in thermoelectricity and water splitting [33,37,102–105]. Kuriyama *et al.* and Shibasaki *et al.* observed a room-temperature thermopower of  $130 \mu\text{VK}^{-1}$  and of  $70 \mu\text{VK}^{-1}$ , respectively, for  $\text{CuRh}_{0.9}\text{Mg}_{0.1}\text{O}_2$  [33,102]. In addition, the former authors reported a figure of merit  $ZT \approx 0.15$  at 1000 K [33].

There were reports on the use of  $\text{CuRhO}_2$  as a photocathode for water splitting under visible light [104,105]. Application in this field benefits from the fact that the band edges are optimally adapted to the water oxidation and reduction redox potentials [104]. Gu *et al.* attributed the stability of the delafossites as photocathodes to the fact that the electron acceptor levels are strongly dominated by the B-type atoms, *i.e.*, the Rh  $d$  levels and pointed to the high sensitivity of the stability and efficiency to even small Cu  $3d$  contributions in this energy range [104]. Thus, there was and still is thus a very high motivation to understand the electronic properties of  $\text{CuRhO}_2$  in detail.

Our calculations were based on the crystal structure data by Oswald *et al.* [106], who determined the lattice constants as  $a = 3.08 \text{ \AA}$  and  $c = 17.09 \text{ \AA}$ . Since these authors did not measure the internal oxygen parameter, we performed a structural optimization leading to a value of  $z_{\text{O}} = 0.10717$ , which was used in all subsequent calculations [37].

The electronic bands along selected high-symmetry lines of the first Brillouin zone of the hexagonal lattice and the partial densities of states (DOS) are displayed in Figs. 16 and 17, respectively. Again, we observe the well known order of states with the crossover from O  $2p$ -dominated bands to sharp transition-metal peaks at about  $-4 \text{ eV}$ . As for the other Cu-based delafossites discussed above, Cu is found in a monovalent  $d^{10}$  configuration in close analogy with the experimental findings with the major  $3d$  peaks well below the valence band edge. The Rh  $4d$  states clearly exhibit splitting into a fully occupied  $t_{2g}$  manifold and empty  $e_g$  bands, which are separated by the fundamental band gap. The calculated value of the latter is about  $0.85 \text{ eV}$ , which is somewhat smaller than the experimental value of  $1.9 \text{ eV}$ . Rh is thus found in a  $d^6$  configuration. The situation is not unlike that of  $\text{CuCrO}_2$ , where, however, only the spin majority

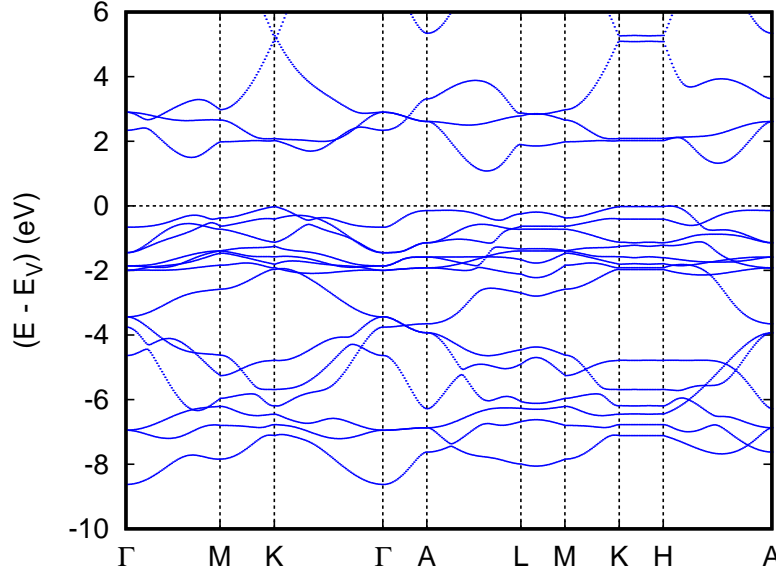


**Figure 16.** Electronic bands of CuRhO<sub>2</sub>. Reprinted with permission from (Phys. Rev. B **80**, 115103 (2009)). Copyright (2009) American Physical Society.

$t_{2g}$  states are occupied and the spin minority  $t_{2g}$  bands are shifted upwards to join the  $e_g$  bands above the band gap.

It is interesting to note the band finite dispersion parallel to  $\Gamma$ -A indicative of considerable three-dimensionality arising from the coupling between the layers. This is contrasted with the barely noticeable dispersion particularly along the line K-H. Yet, both the finite dispersion along  $\Gamma$ -A and the flat bands along K-H have been also observed for the other delafossite materials.

Further insight about the electronic properties is obtained from the optical spectra. The real and imaginary parts of the dielectric function as calculated within linear-response (see Ref. [69] for more details) are shown in Fig. 18. Obviously, the asymmetry between the in-plane and out-of-plane directions is not reflected in the absorption gap following from the imaginary part of the dielectric function. In fact the gap is very close to 0.85 eV in all three directions, which is most likely to exceed the Hund's rule coupling. Therefore, the low-spin  $4d^6$  configuration of  $\text{Rh}^{3+}$  is expected to be the ground state. This is consistent with earlier findings by Singh for  $\text{CuCoO}_2$ , where the Co ions adopt the low-spin  $3d^6$  configuration [89].

Finally, we discuss the thermoelectric properties as evaluated from Boltzmann theory [69,107]. The transport properties are usually expressed in terms of the Onsager transport coefficients (see also Ref. [37] for details). The calculated Seebeck coefficients for different hole doping levels are displayed in Fig. 19. Note that the curves show the average of all components of the diagonal of the respective tensor. As expected, the thermopower strongly decreases with increased hole doping. In addition, it shows the characteristic bending towards smaller increase at high temperatures. As concerns especially the shape of these curves, the results are in almost perfect agreement with the experimental data as shown in Fig. 3 of our own group, the calculations of Usui *et al.* [103], who likewise used the Boltzmann approach, and with the experimental data by Kuriyama *et al.* [33]. Nevertheless, the absolute scaling of the thermopower is at variance both between the calculations and between different experiments. This should be



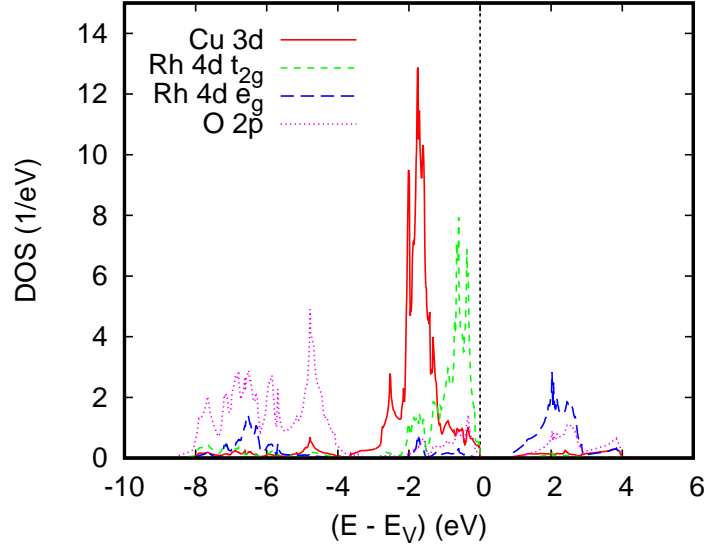


**Figure 17.** Partial densities of states (DOS) of  $\text{CuRhO}_2$ . Selection of the Rh 4d orbitals is relative to the local rotated reference frame, see text. Reprinted with permission from (Phys. Rev. B **80**, 115103 (2009)). Copyright (2009) American Physical Society.

related to the fact that calculated Seebeck coefficients are rather sensitive to details of the crystal structure. In addition, in applying Boltzmann theory, all calculations performed so far used a rigid band picture in order to mimic doping effects. Yet, a doping level of 0.1 holes per formula unit is not a small perturbation. For this reason,  $\text{CuRh}_{0.9}\text{Mg}_{0.1}\text{O}_2$  should be regarded a metal rather than a doped semiconductor as is indeed done in the literature. Nevertheless, in view of these limitations, the above results are remarkably convincing.

## 5. Conclusions and perspectives

It is remarkable that going from  $d^9$  to  $d^{10}$  monovalent cations at the A site of  $\text{A}^+\text{M}^{3+}\text{O}_2$  delafossite the electronic groundstate could switch from “ultra” metallicity as in  $\text{PdCoO}_2$  to semiconductors for  $\text{CuCrO}_2$  or  $\text{CuRhO}_2$ . Accordingly, very different physics in this class of materials can be studied as illustrated by a few examples leading for instance to multiferroicity when A is a  $d^{10}$  monovalent cation in the case of  $\text{CuFeO}_2$  and  $\text{CuCrO}_2$ . Their triangular lattices of localized magnetic moments at the M site is responsible for magnetic frustration which is lifted by antiferromagnetic ordering at rather low Néel temperatures of  $T_N = 16\text{ K}$  and  $T_N = 24\text{ K}$  for  $\text{CuFeO}_2$  and  $\text{CuCrO}_2$ , respectively. For both compounds, the electronic spin-polarized structure calculations are consistent with the experimental observations that the antiferromagnetic semiconductors states are the most stable with high-spin states for  $\text{Fe}^{3+}$  or  $\text{Cr}^{3+}$ . These calculations also reveal energy gaps at  $E_F$  fitting with the poor conducting behavior. However, the limit of these calculations lie in the prediction of the magnetic structure for which subtle changes in the in-plane and out-of-plane exchange energies lead to very different antiferromagnetic structures below  $T_N$  as the 4SL collinear structure in  $\text{CuFeO}_2$  and the incommensurate structures, helicoidal or cycloidal in  $\text{CuCrO}_2$ . Another challenge for the calculations is created by the prediction of the thermoelectric

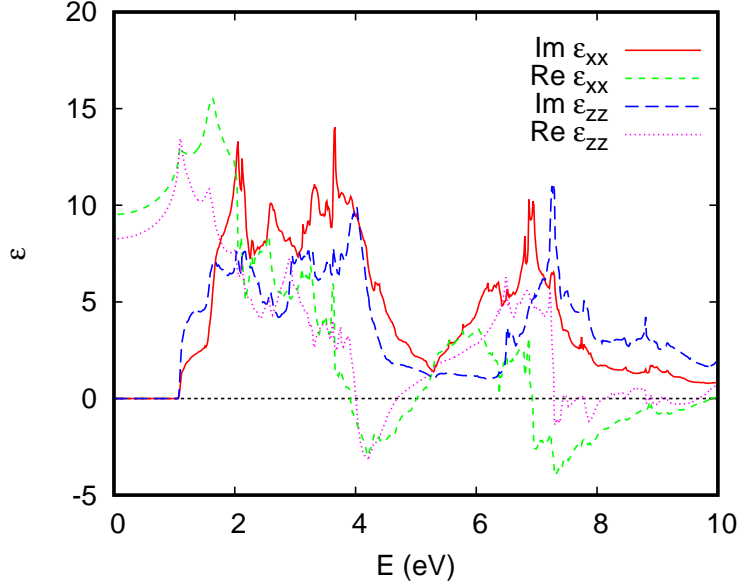


**Figure 18.** Dielectric function of CuRhO<sub>2</sub>.

properties. In these  $d^{10}$  delafossites, substituting  $\text{Mg}^{2+}$  for  $\text{Cr}^{3+}$  or  $\text{Rh}^{3+}$ , leads to interesting thermoelectric properties characteristic of p-type materials which can be described as doped semiconductors in the case of  $\text{CuCr}_{1-x}\text{Mg}_x\text{O}_2$  but as metals in the case of heavily doped  $\text{CuRh}_{1-x}\text{Mg}_x\text{O}_2$  ( $x \simeq 0.1$ ).

Let us also remark that the band structure of delafossites entails Dirac cones, especially the one of CuRhO<sub>2</sub> [37]. Since they are far away from the Fermi energy they do not seem to have much influence on the physical properties. Yet, the Dirac cones could be brought closer to the Fermi energy in a capacitor geometry through the use of gate biases, see, *e.g.*, [108,109], to provide us with the first oxide topological insulator.

The large splitting of the 3d (or 4d)  $t_{2g}$  and  $e_g$  orbitals at  $E_F$  in CuCrO<sub>2</sub> (or CuRhO<sub>2</sub>) which accounts for the physical properties of these delafossites is in marked contrast with the incomplete band filling of  $d^9$  Pd<sup>+</sup> in PdCoO<sub>2</sub> or PdCrO<sub>2</sub> with Pd 4d states almost exclusively responsible for electrical conductivity. More particularly, the  $d_{xy, x^2-y^2}$  orbitals add the largest contribution to the DOS at  $E_F$ . It results a simple Fermi surface, characteristic of quasi-2D electronic states. Thus, PdCoO<sub>2</sub> can be regarded as a textbook example of quasi-2D metals, which are also of high interest as paradigmatic candidates for angle-resolved photoemission spectroscopy line shape studies [110]. The stacking of Pd conducting layers alternating with a quasi-insulating CoO<sub>2</sub> layers leads to effects rarely seen in condensed matter. Although the 2D character is reflected in the anisotropic resistivities, the thermal conductivity  $\kappa$  being dominated by the lattice contribution,  $\kappa$  is much less anisotropic. As a result, PdCoO<sub>2</sub> is a metal with anomalously large  $\kappa$  values as compared to the values reported for noble metals. The thermoelectric power follows the prediction of the free-electron theory and, for PdCrO<sub>2</sub>, where the “insulating layer” contains a paramagnetic cations ( $\text{Cr}^{3+}$ ;  $S=3/2$ ), the physics becomes more complex. For instance, the Nernst coefficient is found to become large below  $T_N$  with a very large sensitivity to the magnetic field. It must be also emphasized that these metallic delafossites belong also to the Weyl semimetals, a class of topological materials. This hypothesis has been put forward to explain the negative longitudinal magnetoresistance. Finally, growth of thicker crystals is needed

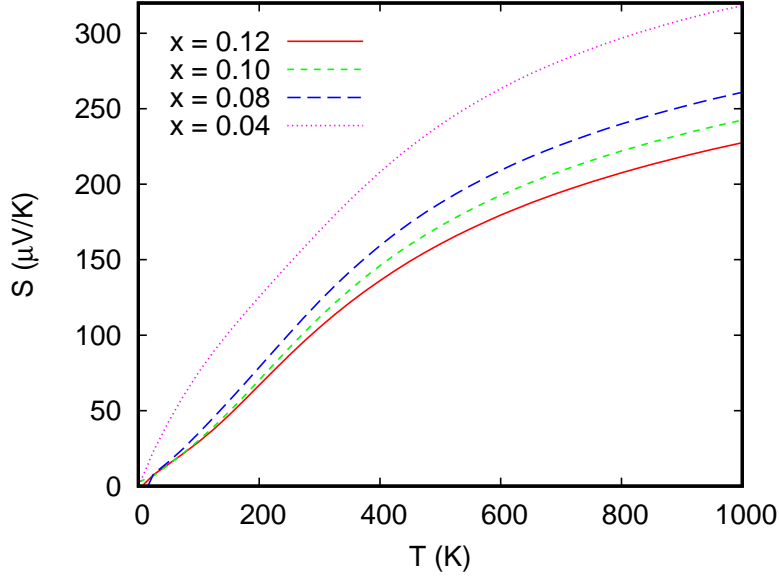


**Figure 19.** Thermopower  $S$  of  $\text{CuRhO}_2$  for different hole doping levels. The curves display the average of all three diagonal components of the tensor.

for testing the prediction of high Seebeck coefficient along the transverse direction ( $S \simeq 200 \mu\text{V K}^{-1}$  along the  $c$  axis) together with a moderate out-of-plane resistivity. However, the  $\kappa$  measurement revealing very large values even for the transverse direction are not in favor of any applicability of these material in thermoelectricity based waste-heat recovery.

Following the graphene original physics, the delafossites compounds, which 2D structure can be described as a natural 1:1 epitaxy of a metal  $d^9$  or insulator  $d^{10}$  metal layers with a  $\text{MO}_2$  layer of the  $\text{CdI}_2$ -type, which can be diamagnetic or paramagnetic at room temperature with possibly an antiferromagnetic order at low  $T$ , offer a broad range of combinations to generate new physical properties. In that respect, there remains room for the chemists to produce materials of original compositions, to grow larger crystals to characterize all anisotropic properties — including the thermopower and thermal conductivity — and for the physicist, beyond all measurements still to be done, to improve the modeling of these properties.

Finally, it must be emphasized that the selected examples described in this review paper represent only a few compounds among a very broad family of delafossites. Looking beyond the oxides at compounds crystallizing in similar structures, it must be also mentioned that there exists many layered  $\text{AMX}_2$  compounds for other chalcogen ions ( $\text{X}=\text{S}, \text{Se}, \text{Te}$ ) for which the physics is also very exciting as complex antiferromagnetism in  $\text{AgCrS}_2$  and  $\text{AgCrSe}_2$  or the photovoltaic effects in CIGS ( $\text{CuGa}_{1-x}\text{In}_x\text{Se}_2$ ). However, to the best of our knowledge, delafossite-like sulfides or selenides with metallicity as good as that of  $\text{PdCoO}_2$  keep on escaping synthesis. Again, this outlines the importance of oxides to generate unusual properties.

## 6. Acknowledgements

The authors are grateful for collaborations and discussions with numerous colleagues, especially E. Guilmeau, C. Hicks, K.-H. Höck, T. Kopp, S. Kremer, D. Ledue, C. Mar-

tin, M. Poienar, W. C. Sheets, and Ch. Simon. The authors acknowledge the financial support of the French Agence Nationale de la Recherche (ANR), through the program Investissements d'Avenir (ANR-10-LABX-09-01), LabEx EMC3, and the Deutsche Forschungsgemeinschaft through SFB 484 and TRR 80. Figs. 1 and 9 were generated using the XCrysDen software (Ref. [111]).

## Bibliography

### References

- [1] Imada M, Fujimori A and Tokura Y. Metal-insulator transitions. *Rev. Mod. Phys.* 1998; 70: 1039.
- [2] McWhan DB, Menth A, Remeika JP, Brinkman WF and Rice TM. Metal-Insulator Transitions in Pure and Doped  $V_2O_3$ . *Phys. Rev. B* 1973; 7: 1920.
- [3] Held K, Keller G, Eyert V, Vollhardt D, Anisimov VI, Mott-Hubbard Metal-Insulator Transition in Paramagnetic  $V_2O_3$ : An LDA+DMFT(QMC) Study. *Phys. Rev. Lett.* 2001; 86: 5345.
- [4] Limelette P, Georges A, Jérôme D, Wzietek P, Metcalf P and Honig JM. Universality and Critical Behavior at the Mott Transition. *Science* 2003; 302: 89.
- [5] Grygiel C, Simon Ch, Mercey B, Prellier W, Frésard R and Limelette P. Thickness-dependence of the electronic properties in  $V_2O_3$  thin films. *Appl. Phys. Lett.* 2007; 91: 262103.
- [6] von Helmolt R, Wecker J, Holzapfel B, Schultz L and Samwer K. Giant negative magnetoresistance in perovskitelike  $La_{2/3}Ba_{1/3}MnO_x$  ferromagnetic films. *Phys. Rev. Lett.* 1993; 71: 2331.
- [7] Tomioka Y, Asamitsu A, Moritomo Y, Kuwahara H, and Tokura Y. Collapse of a Charge-Ordered State under a Magnetic Field in  $Pr_{1/2}Sr_{1/2}MnO_3$ . *Phys. Rev. Lett.* 1995; 74: 5108.
- [8] Raveau B, Maignan A and Caignaert V. Spectacular Giant Magnetoresistance Effects in the Polycrystalline Perovskite  $Pr_{0.7}Sr_{0.05}Ca_{0.25}MnO_{3-\delta}$ . *J. Solid State Chem.* 1995; 117: 424.
- [9] Maignan A, Simon C, Caignaert V and Raveau B. Giant magnetoresistance ratios superior to  $10^{11}$  in manganese perovskites. *Solid State Commun.* 1995; 96: 623.
- [10] Eyert V, Laschinger C, Kopp T and Frésard R. Extended moment formation and magnetic ordering in the trigonal chain compound  $Ca_3Co_2O_6$ . *Chem. Phys. Lett.* 2004; 385: 249.
- [11] Frésard R, Laschinger C, Kopp T and Eyert V. The Origin of Magnetic Interactions in  $Ca_3Co_2O_6$ . *Phys. Rev. B* 2004; 69: 140405(R).
- [12] Wu H, Haverkort MW, Hu Z, Khomskii DI, and Tjeng LH. Nature of Magnetism in  $Ca_3Co_2O_6$ . *Phys. Rev. Lett.* 2005; 95: 186401.
- [13] Terasaki I, Sasago Y, and Uchinokura K. Large thermoelectric power in  $NaCo_2O_4$  single crystals. *Phys. Rev. B* 1997; 56: R12685.
- [14] Masset AC, Michel C, Maignan A, Hervieu M, Toulemonde O, Studer F and Raveau B. Misfit-layered cobaltite with an anisotropic giant magnetoresistance:  $Ca_3Co_4O_9$ . *Phys. Rev. B* 2000; 62: 166.
- [15] Friedel C. Sur une combinaison naturelle des oxydes de fer et de cuivre, et sur la reproduction de l'atacamite. *Sciences Academy* 1873; 77: 211.
- [16] Shannon RD, Rogers DB and Prewitt CT. Chemistry of Noble Metal Oxides. I. Syntheses and Properties of  $ABO_2$  Delafossite Compounds. *Inorg. Chem.* 1971; 10: 713; Prewitt CT, Shannon RD and Rogers DB. Chemistry of Noble Metal Oxides. II. Crystal Structure of  $PtCoO_2$ ,  $PdCoO_2$ ,  $CuFeO_2$ ,  $AgFeO_2$ . *Inorg. Chem.* 1971; 10: 719; Rogers DB, Shannon RD and Prewitt CT. Chemistry of Noble Metal Oxides. III. Electrical Transport Properties and Crystal Chemistry of  $ABO_2$  Compounds with Delafossite Structure. *Inorg. Chem.*

- 1971; 10: 723.
- [17] Tanaka M, Hasegawa M, Higuchi T, Tsukamoto T, Tezuka Y, Shin S. and Takei H. Origin of the metallic conductivity in  $\text{PdCoO}_2$  with delafossite structure. *Physica B* 1998; 245: 157.
  - [18] Marquardt MA, Ashmore NA and Cann DP. Crystal chemistry and electrical properties of the delafossite structure. *Thin Solid Films* 2006; 496: 146.
  - [19] Kawazoe H, Yasukawa M, Hyodo H, Kurita M, Yanagi H and Hosono H. P-type electrical conduction in transparent thin films of  $\text{CuAlO}_2$ . *Nature* 1997; 389: 939.
  - [20] Hasegawa M, Tanaka M, Yagi T, Takei H and Inoue A. Compression behavior of the delafossite-type metallic oxide  $\text{PdCoO}_2$  below 10 GPa. *Solid State Commun.* 2003: 128; 303.
  - [21] Wawrzyńska E, Coldea R, Wheeler EM, Mazin II, Johannes MD, Sörgel T, Jansen M, Ibberson RM and Radaelli PG. Orbital Degeneracy Removed by Charge Order in Triangular Antiferromagnet  $\text{AgNiO}_2$ . *Phys. Rev. Lett.* 2007; 99: 157204.
  - [22] Kang J-S, Lee SS, Kim G, Lee HJ, Song HK, Shin YJ, Han SW, Hwang C, Jung MC, Shin HJ, Kim BH, Kwon SK and Min BI. Valence and spin states in delafossite  $\text{AgNiO}_2$  and the frustrated Jahn-Teller system  $\text{ANiO}_2$  ( $\text{A}=\text{Li}, \text{Na}$ ). *Phys. Rev. B* 2007; 76: 195122.
  - [23] Oohara Y, Mitsuda S, Yoshizawa H, Yaguchi N, Kuriyama H, Asano T and Mekata M. Magnetic Phase Transition in  $\text{AgCrO}_2$ . *J. Phys. Soc. Jpn.* 1994; 63: 847.
  - [24] Seki S, Onose Y and Tokura Y. Spin-driven ferroelectricity in triangular lattice antiferromagnets  $\text{ACrO}_2$  ( $\text{A}=\text{Cu}, \text{Ag}, \text{Li}, \text{or Na}$ ). *Phys. Rev. Lett.* 2008; 101: 067204.
  - [25] Hasegawa M, Inagawa I, Tanaka M, Shirotnani I, Takei H. Thermoelectric power of delafossite-type metallic oxide  $\text{PdCoO}_2$ . *Solid State Commun.* 2002; 121: 203.
  - [26] Mackenzie AP. The properties of ultrapure delafossite metals. *Rep. Prog. Phys.* 2017; 80: 0325Q01.
  - [27] Doumerc JP, Wichainchai A, Ammar A, Pouchard M and Hagenmuller P. On the formation of delafossites type oxides and solid solutions. *Mat. Res. Bull.* 1986; 21: 745.
  - [28] Poienar M, Damay F, Martin C, Hardy V, Maignan A, André G. Structural and magnetic properties of  $\text{CuCr}_{1-x}\text{Mg}_x\text{O}_2$  by neutron powder diffraction. *Phys. Rev. B* 2009; 79: 014412.
  - [29] Albaalbaky A, Kvashnin YO, Ledue D, Patte R, Frésard R. Magnetoelectric properties of the multiferroic  $\text{CuCrO}_2$  studied by means of ab initio calculations and Monte Carlo simulations. *Phys. Rev. B* 2017; 96: 064431.
  - [30] Okuda T, Jufuku N, Hidaka S and Terada N. Magnetic, transport, and thermoelectric properties of the delafossite oxides  $\text{CuCr}_{1-x}\text{Mg}_x\text{O}_2$  ( $0 \leq x \leq 0.04$ ). *Phys. Rev. B* 2005; 72: 144403.
  - [31] Ono Y, Satoh K, Nozaki T and Kajitani T. Structural, magnetic and transport properties of delafossite - type oxide  $\text{CuCr}_{1-x}\text{Mg}_x\text{O}_2$  ( $0 \leq x \leq 0.05$ ). *Jpn. J. Appl. Phys.* 2007; 46: 1071.
  - [32] Koshibae W, Tsutsui K and Maekawa S, Thermopower in cobalt oxides. *Phys. Rev. B* 2000; 62: 6869.
  - [33] Kuriyama K, Nohara M, Sasagawa T, Tabuko K, Mizokawa F, Kimura K and Takagi H, High temperature thermoelectric properties of delafossite oxides  $\text{CuRh}_{1-x}\text{Mg}_x\text{O}_2$ . *Proc. 25th Int. Conf. Thermoelectrics* (IEEE, Piscataway, 2006), p. 97.
  - [34] Nozaki T, Hayashi K and Kajitani T, Thermoelectric properties of delafossite type oxide  $\text{CuFe}_{1-x}\text{Ni}_x\text{O}_2$  ( $0 \leq x \leq 0.05$ ). *J. Chem. Eng. Jpn.* 2007; 40: 1205.
  - [35] Maignan A, Martin C, Frésard R, Eyert V, Guilmeau E, Hébert S, Poienar M and Pelloquin D. On the strong impact of doping in the triangular antiferromagnet  $\text{CuCrO}_2$ . *Solid State Commun.* 2009; 149: 962.
  - [36] Guilmeau E, Poienar M, Kremer S, Marinel S, Hébert S, Frésard R and Maignan A. Mg substitution in  $\text{CuCrO}_2$  delafossite compounds. *Solid State Commun.* 2011; 151: 1798.
  - [37] Maignan A, Eyert V, Martin C, Kremer S, Frésard R, and Pelloquin D. Electronic structure and thermoelectric properties of  $\text{CuRh}_{1-x}\text{Mg}_x\text{O}_2$ . *Phys. Rev. B* 2009; 80: 115103.
  - [38] Guilmeau E, Maignan A. and Martin C., Thermoelectric oxides: effect of doping in de-

- lafossites and zinc oxides. *J. Electron. Mater.* 2009; 38: 1104.
- [39] Kremer S and Frésard R. Thermoelectric transport properties of an apparent Fermi liquid: Relation to an analytic anomaly in the density of states and application to hole-doped delafossites. *Ann. Phys. (Berlin)* 2012; 524: 21.
  - [40] Terada N. Spin and orbital orderings behind multiferroicity in delafossite and related compounds. *J. Phys.: Condens. Mater.* 2014; 26: 453202.
  - [41] Kushwaha P, Sunko V, Moll PJW, Bawden L, Riley JM, Nandi N, Rosner H, Schmidt MP, Arnold F, Hassinger E, Kim TK, Hoesch M, Mackenzie AP and King PDC. Nearly free electrons in a 5d delafossite oxide metal. *Sci. Adv.* 2015; 1: 1500692.
  - [42] Kushwaha P, Borrmann H, Khim S, Rosner H, Moll PJW, Sokolov DA, Sunko V, Grin Y, and Mackenzie AP. Single Crystal Growth, Structure, and Electronic Properties of Metallic Delafossite PdRhO<sub>2</sub>. *Cryst. Growth Des.* 2017; 17: 4144.
  - [43] Hicks CW, Gibbs AS, Mackenzie AP, Takatsu H, Maeno Y and Yelland EA. Quantum Oscillations and High Carrier Mobility in the Delafossite PdCoO<sub>2</sub>. *Phys. Rev. Lett.* 2012; 109: 116401.
  - [44] Noh HJ, Jeong J, Jeong J, Cho EJ, Kim SB, Kim K, Min BI, and Kim HD. Anisotropic Electric Conductivity of Delafossite PdCoO<sub>2</sub> Studied by Angle-Resolved Photoemission Spectroscopy. *Phys. Rev. Lett.* 2009; 102: 256404.
  - [45] Ok JM, Jo YJ, Kim K, Shishidou T, Choi ES, Noh HJ, Oguchi T, Min BI and Kim JS. Quantum Oscillations of the Metallic Triangular-Lattice Antiferromagnet PdCrO<sub>2</sub>. *Phys. Rev. Lett.* 2013; 111: 176405.
  - [46] Hicks CW, Gibbs AS, Zhao L, Kushwaha P, Borrmann H, Mackenzie AP, Takatsu H, Yonezawa S, Maeno M and Yelland EA. Quantum oscillations and magnetic reconstruction in the delafossite PdCrO<sub>2</sub>. *Phys. Rev. B* 2015; 92: 014425.
  - [47] Shin YJ, Doumerc JP, Dordor P, Pouchard M and Hagenmuller P. Preparation and Physical Properties of the Delafossite-Type Solid Solutions AgCo<sub>x</sub>Ni<sub>1-x</sub>O<sub>2</sub> ( $0 \leq x \leq 0.5$ ). *J. Solid State Chem.* 1993; 107: 194.
  - [48] Takatsu H and Maeno Y. Single crystal growth of the metallic triangular-lattice antiferromagnet PdCrO<sub>2</sub>. *J. Cryst. Growth* 2010; 312: 3461.
  - [49] Takatsu H, Onezawa SY, Ouri SM, Nakatsuji S, Anaka KT and Maeno Y. Roles of High-Frequency Optical Phonons in the Physical Properties of the Conductive Delafossite PdCoO<sub>2</sub>. *J. Phys. Soc. Jpn.* 2007; 76: 104701.
  - [50] Daou R, Frésard R, Hébert S and Maignan A. Large anisotropic thermal conductivity of the intrinsically two-dimensional metallic oxide PdCoO<sub>2</sub>. *Phys. Rev. B* 2015; 91: 041113(R).
  - [51] Moll PJW, Kushwaha P, Nandi N, Schmidt B and Mackenzie AP. Evidence for hydrodynamic electron flow in PdCoO<sub>2</sub>. *Science* 2016; 351: 1061.
  - [52] Kikugawa N, Goswami P, Kiswandhi A, Choi ES, Graf D, Baumbach RE, Brooks JS, Sugii K, Iida Y, Nishio M, Uji S, Terashima T, Rourke PMC, Hussey NE, Takatsu H, Yonezawa S, Maeno Y and Balicas L. Interplanar coupling-dependent magnetoresistivity in high-purity layered metals. *Nat. Commun.* 2016; 7: 10903.
  - [53] Takatsu H, Yoshizawa H, Yonezawa S, Maeno Y. Critical behavior of the metallic triangular-lattice Heisenberg antiferromagnet PdCrO<sub>2</sub>. *Phys. Rev. B* 2009; 79: 104424.
  - [54] Billington D, Ernsting D, Millichamp TE, Lester C, Dugdale SB, Kersh D, Duffy JA, Giblin SR, Taylor JW, Manuel P, Khalyavin DD and Takatsu H. Magnetic frustration, short-range correlations and the role of the paramagnetic Fermi surface of PdCrO<sub>2</sub>. *Sci. Rep.* 2015; 5: 12428.
  - [55] Takatsu H, Ishikawa JJ, Yonezawa S, Yoshino H, Shishidou T, Oguchi T, Murata K and Maeno Y. Extremely Large Magnetoresistance in the Nonmagnetic Metal PdCoO<sub>2</sub>. *Phys. Rev. Lett.* 2013; 111: 056601.
  - [56] Goswami P, Pixley JH and Das Sarma S. Axial anomaly and longitudinal magnetoresistance of a generic three-dimensional metal. *Phys. Rev. B* 2015; 92: 075205.
  - [57] Takatsu H, Yonezawa S, Fujimoto S and Maeno Y. Unconventional Anomalous Hall Effect in the Metallic Triangular-Lattice Magnet PdCrO<sub>2</sub>. *Phys. Rev. Lett.* 2010; 105: 137201.



- [58] Daou R, Frésard R, Hébert S and Maignan A. Impact of short-range order on transport properties of the two-dimensional metal PdCrO<sub>2</sub>. Phys. Rev. B 2015; 92: 245115.
- [59] Ong KP, Singh DJ, Wu P. Unusual Transport and Strongly Anisotropic Thermopower in PtCoO<sub>2</sub> and PdCoO<sub>2</sub>. Phys. Rev. Lett. 2010; 104: 176601.
- [60] Zhou C, Birner S, Tang Y, Heinselman K and Grayson M. Driving Perpendicular Heat Flow: ( $p \times n$ )-Type Transverse Thermoelectrics for Microscale and Cryogenic Peltier Cooling. Phys. Rev. Lett. 2013; 110: 227701.
- [61] Arsenijević S, Ok JM, Robinson P, Ghannadzadeh S, Katsnelson MI, Kim JS and Hussey NE. Anomalous Magnetothermopower in a Metallic Frustrated Antiferromagnet. Phys. Rev. Lett. 2016; 116: 087202.
- [62] Hohenberg P and Kohn W. Inhomogeneous Electron Gas. Phys. Rev. 1964; 136: B864.
- [63] Kohn K and Sham LJ. Self-Consistent Equations Including Exchange and Correlation Effects. Phys. Rev. 1965; 140: A1133.
- [64] Wimmer E, Christensen M, Eyert V, Wolf W, Reith D, Rozanska X, Freeman C, and Saxe P. Computational Materials Engineering: Recent Applications of VASP in the MedeA® Software Environment. J. Korean Ceram. Soc. 2016; 53: 263.
- [65] Rozanska X, Christensen M, Wolf W, Eyert V, Mavromaras A, Leblanc B, Freeman C, Saxe P, and Wimmer E. L'apport de la chimie et de la physique théoriques dans la transition vers les énergies renouvelables. L'actualité chimique 2016; 408-409: 19.
- [66] Eyert V, Frésard R and Maignan A. On the metallic conductivity of the delafossites PdCoO<sub>2</sub> and PtCoO<sub>2</sub>. Chem. Mater. 2008; 20: 2370.
- [67] Eyert V, Frésard R and Maignan A. Long-range magnetic order and spin-lattice coupling in the delafossite CuFeO<sub>2</sub>. Phys. Rev. B 2008; 78: 052402.
- [68] Eyert V. Basic notions and applications of the augmented spherical wave method. Int. J. Quantum Chem. 2000; 77: 1007.
- [69] Eyert V. The Augmented Spherical Wave Method. Lect. Notes Phys. 2012; 849. (Springer, Berlin Heidelberg 2012).
- [70] Seshadri R, Felser C, Thieme K and Tremel W. Metal-Metal Bonding and Metallic Behavior in Some ABO<sub>2</sub> Delafossites. Chem. Mater. 1998; 10: 2189.
- [71] Okabe H, Matoba M, Kyomen T and Itoh M. Magnetic property and electronic structure of itinerant Pd<sub>x</sub>Co<sub>y</sub>O<sub>2</sub> magnets. J. Appl. Phys. 2003; 93: 7258.
- [72] Higuchi T, Tsukamoto T, Tanaka M, Ishii H, Kanai K, Tezuka Y, Shin S and Takei H. Photoemission study on PdCoO<sub>2</sub>. J. Electr. Spectr. Rel. Phen. 1998; 92; 71.
- [73] Higuchi T, Hasegawa M, Tanaka M, Takei H, Shin S and Tsukamoto T. Unoccupied Electronic State of Delafossite-Type PdCoO<sub>2</sub> Single Crystal Probed Using Inverse Photoemission Spectroscopy. Jap. J. Appl. Phys. 2004; 43: 699.
- [74] Ong KP, Zhang J, Tse JS, and Wu P. Origin of anisotropy and metallic behavior in delafossite PdCoO<sub>2</sub>. Phys. Rev. B 2010; 81: 115120.
- [75] Gruner ME, Eckern U, and Pentcheva R. Impact of strain-induced electronic topological transition on the thermoelectric properties of PtCoO<sub>2</sub> and PdCoO<sub>2</sub>. Phys. Rev. B 2015; 92: 235140.
- [76] Noh H-J, Jeong J, Jeong J, Sung H, Park KJ, Kim J-Y, Kim H-D, Kim SB, Kim K, and Min BI. Orbital character of the conduction band of delafossite PdCoO<sub>2</sub> studied by polarization-dependent soft x-ray absorption spectroscopy. Phys. Rev. B 2009; 80: 073104.
- [77] Kimura K, Nakamura H, Kimura S, Hagiwara M and Kimura T. Tuning Ferroelectric Polarization Reversal by Electric and Magnetic Fields in CuCrO<sub>2</sub>. Phys. Rev. Lett. 2009; 103: 107201.
- [78] Muir AH and Wiedersich M. An investigation of CuFeO<sub>2</sub> by the Mössbauer effect. J. Phys. Chem. Solids 1967; 28: 65.
- [79] Mekata M, Yaguchi N, Takagi T, Mitsuda S and Yoshizawa H. Magnetic ordering in delafossite CuFeO<sub>2</sub>. J. Magn. Magn. Mater. 1992; 104: 823.
- [80] Mekata M, Yaguchi N, Takagi T, Sugino T, Mitsuda S, Yoshizawa H, Hosoi N and Shinjo T. Successive Magnetic Ordering in CuFeO<sub>2</sub> –A New Type of Partially Disordered Phase in a Triangular Lattice Antiferromagnet–. J. Phys. Soc. Jpn. 1993; 62: 4474.

- [81] Petrenko OA, Balakrishnan G, Lees MR, McK. Paul D and Hoser A. High-magnetic-field behavior of the triangular-lattice antiferromagnet  $\text{CuFeO}_2$ . *Phys. Rev. B* 2000; 62: 8983.
- [82] Kimura T, Lashley JC and Ramirez AP. Inversion-symmetry breaking in the noncollinear magnetic phase of the triangular-lattice antiferromagnet  $\text{CuFeO}_2$ . *Phys. Rev. B* 2006; 73: 220401(R).
- [83] Ye F, Ren Y, Huang Q, Fernandez-Baca JA, Dai P, Lynn JW, and Kimura T. Spontaneous spin-lattice coupling in the geometrically frustrated triangular lattice antiferromagnet  $\text{CuFeO}_2$ . *Phys. Rev. B* 2006; 73: 220404(R).
- [84] Ye F, Fernandez-Baca JA, Fishman RS, Ren Y, Kang HJ, Qiu Y, and Kimura T. Magnetic Interactions in the Geometrically Frustrated Triangular Lattice Antiferromagnet  $\text{CuFeO}_2$ . *Phys. Rev. Lett.* 2007; 99: 157201.
- [85] Seki S, Yamasaki Y, Shiomi Y, Iguchi S, Onose Y and Tokura Y. Impurity-doping-induced ferroelectricity in the frustrated antiferromagnet  $\text{CuFeO}_2$ . *Phys. Rev. B* 2007; 75: 100403(R).
- [86] Ruttapanun C, Wichainchai A, Prachamon W, Yangthaisong A, Charoenphakdee A, and Seetawan T. Thermoelectric properties of  $\text{Cu}_{1-x}\text{Pt}_x\text{FeO}_2$  ( $0.0 \leq x \leq 0.05$ ) delafossite-type transition oxide. *J. Alloys Compd.* 2011; 509: 4588.
- [87] Galakhov VR, Poteryaev AI, Kurmaev EZ, Anisimov VI, Bartkowski S, Neumann M, Lu ZW, Klein BM, and Zhao T-R. Valence-band spectra and electronic structure of  $\text{CuFeO}_2$ . *Phys. Rev. B* 1997; 56: 4584.
- [88] Ong KP, Bai K, Blaha P and Wu P. Electronic Structure and Optical Properties of  $\text{AFeO}_2$  ( $\text{A} = \text{Ag}, \text{Cu}$ ) within GGA Calculations. *Chem. Mater.* 2007; 19: 634.
- [89] Singh DJ. Electronic and thermoelectric properties of  $\text{CuCoO}_2$ : Density functional calculations. *Phys. Rev. B* 2007; 76: 085110.
- [90] Zhong C, Cao H, Fang J, Jiang X, Ji X, and Dong Z. Spin-lattice coupling and helical-spin driven ferroelectric polarization in multiferroic  $\text{CuFeO}_2$ . *Appl. Phys. Lett.* 2010; 97: 094103.
- [91] Hiraga H, Makino T, Fukumura T, Weng H, and Kawasaki M. Electronic structure of the delafossite-type  $\text{CuMO}_2$  ( $\text{M} = \text{Sc}, \text{Cr}, \text{Mn}, \text{Fe}, \text{and Co}$ ): Optical absorption measurements and first-principles calculations. *Phys. Rev. B* 2011; 84: 041411.
- [92] Kadowaki H, Kikuchi H and Ajiro Y. Neutron Powder Diffraction Study of the 2-dimensional Triangular Lattice Antiferromagnet  $\text{CuCrO}_2$ . *J. Phys.: Condens. Matter* 1990; 2: 4485.
- [93] Soda M, Kimura K, Kimura T, Matsuura M and Hirota K. Electric Control of Spin Helicity in Multiferroic Triangular Lattice Antiferromagnet  $\text{CuCrO}_2$  with Proper-Screw Order. *J. Phys. Soc. Jpn.* 2009; 78: 124703.
- [94] Kimura K, Otani, T, Nakamura H, Wakabayashi Y, and Kimura T. Lattice Distortion Coupled with Magnetic Ordering in a Triangular Lattice Antiferromagnet  $\text{CuCrO}_2$ . *J. Phys. Soc. Jpn.* 2009; 78: 113710.
- [95] Pachoud E, Singh K, Bréard Y, Martin C, André G, Hardy V, Simon C, and Maignan A. Magnetic dilution and steric effects in the multiferroic delafossite  $\text{CuCrO}_2$ . *Phys. Rev. B* 2012; 86: 054437.
- [96] Crottaz O, Kubel F and Schmid H. Preparation of Trigonal and Hexagonal Cuprous Chromite and Phase Transition Study Based on Single Crystal Structure Data. *J. Solid State Chem.* 1996; 122: 247.
- [97] Scanlon DO, Walsh A, Morgan BJ, Watson GW, Payne DJ, and Egdell RG. Effect of Cr substitution on the electronic structure of  $\text{CuAl}_{1-x}\text{Cr}_x\text{O}_2$ . *Phys. Rev. B* 2009; 79: 035101.
- [98] Scanlon DO, Godinho KG, Morgan BJ, and Watson GW. Understanding conductivity anomalies in  $\text{Cu}^I$ -based delafossite transparent conducting oxides: Theoretical insights. *J. Chem. Phys.* 2010; 132: 024707.
- [99] Scanlon DO and Watson GW. Understanding the p-type defect chemistry of  $\text{CuCrO}_2$ . *J. Mater. Chem.* 2011; 21: 3655.
- [100] Yokobori T, Okawa M, Konishi K, Katayama K, Oozono S, Shinmura T, Okuda T, Wadati H, Sakai E, Ono K, Kumigashira H, Oshima M, Sugiyama T, Ikenaga E, Hamada

- N, and Saitoh T. Electronic structure of the hole-doped delafossite oxides  $\text{CuCr}_{1-x}\text{Mg}_x\text{O}_2$ . Phys. Rev. B 2013; 87: 195124.
- [101] Jiang X-F, Liu X-F, Wu Y-Z, Han J-R. Exchange coupling and helical spin order in the triangular lattice antiferromagnet  $\text{CuCrO}_2$  using first principles. Chin. Phys. B 2012; 21: 077502.
  - [102] Shibasaki S, Kobayashi W, and Terasaki I. Transport properties of the delafossite Rh oxide  $\text{Cu}_{1-x}\text{Ag}_x\text{Rh}_{1-y}\text{Mg}_y\text{O}_2$ : Effect of Mg substitution on the resistivity and Hall coefficient. Phys. Rev. B 2006; 74: 235110.
  - [103] Usui H, Arita R, and Kuroki K. First-principles study on the origin of large thermopower in hole-doped  $\text{LaRhO}_3$  and  $\text{CuRhO}_2$ . J. Phys.: Condens. Matter 2009; 21: 064223.
  - [104] Gu J, Yan Y, Krizan JW, Gibson QD, Detweiler ZM, Cava RJ, and Bocarsly AB. p-Type  $\text{CuRhO}_2$  as a Self-Healing Photoelectrode for Water Reduction under Visible Light. J. Am. Chem. Soc. 2014; 136: 830.
  - [105] Toyoda K, Hinogami R, Miyata N, and Aizawa M. Calculated Descriptors of Catalytic Activity for Water Electrolysis Anode: Application to Delafossite Oxides. J. Phys. Chem. 2015; 119: 6495.
  - [106] Oswald HR, Kuhn P and Reller A. Bimetallic phases from reduction of delafossite-type oxides in hydrogen. Solid State Ionics 1989; 32/33: 528.
  - [107] Allen PB. Boltzmann theory and resistivity of metals. In: *Quantum Theory of Real Materials*, ed by Chelikowsky JR and Louie SG (Kluwer, Boston 1996) pp 219–250.
  - [108] Thiel S, Hammerl G, Schmehl A, Schneider CW and Mannhart J. Tunable quasi-two-dimensional electron gases in oxide heterostructures. Science 2006; 313: 1942.
  - [109] Steffen K, Kopp T and Frésard R. Capacitance and compressibility of heterostructures with strong electronic correlations. Phys. Rev. B 2017; 95: 035143.
  - [110] Claessen R, Anderson RO, Gweon G-H, Allen JW, Ellis WP, Janowitz C, Olson CG, Shen ZX, Eyert V, Skibowski M, Friemelt K, Bucher E, and Hüfner SH. Complete band structure determination of the quasi-two-dimensional Fermi-liquid reference compound  $\text{TiTe}_2$ . Phys. Rev. B 1996; 54: 2453.
  - [111] Kokalj A. Computer graphics and graphical user interfaces as tools in simulations of matter at the atomic scale. Comp. Mater. Sci. 2003; 28: 155.